Detection of Reconnection Signatures in Solar
Flares

THESIS

Taylor R. Whitney, 1st Lt, USAF

AFIT-ENP-MS-20-M-121

DEPARTMENT OF THE AIR FORCE
AIR UNIVERSITY

AIR FORCE INSTITUTE OF TECHNOLOGY

Wright-Patterson Air Force Base, Ohio

AFIT-ENP-MS-20-M-121

DETECTION OF RECONNECTION SIGNATURES

IN SOLAR FLARES

THESIS

Presented to the Faculty

Department of Engineering Physics

Graduate School of Engineering and Management

Air Force Institute of Technology

Air University

Air Education and Training Command

in Partial Fulfillment of the Requirements for the

Degree of Master of Science in Applied Physics

Taylor R. Whitney, B.S.

1st Lt, USAF

March 2020

DETECTION OF RECONNECTION SIGNATURES

IN SOLAR FLARES

THESIS

Taylor R. Whitney, B.S.
1st Lt, USAF

Committee Membership:

Robert D. Loper, Ph.D.
Chair

Maj Daniel J. Emmons, Ph.D.
Member

AFIT-ENP-MS-20-M-121

Abstract

Solar flare forecasting is limited by the current understanding of mechanisms that govern magnetic reconnection, the main physical phenomenon associated with these events. As a result, forecasting relies mainly on climatological correlations to historical events rather than the underlying physics principles. Solar physics models place the neutral point of the reconnection event in the solar corona. Correspondingly, studies of photospheric magnetic fields indicate changes during solar flares— particularly in relation to the field helicity—on the solar surface as a result of the associated magnetic reconnection. This study utilizes data from the Solar Dynamics Observatory (SDO) Helioseismic and Magnetic Imager (HMI) and SpaceWeather HMI Active Region Patches (SHARPs) to analyze full vector-field component data of the photospheric magnetic field during solar flares within a large HMI dataset (May 2010 through September 2019). This analysis is then used to identify and compare trends in the different categories of flare strengths and determine indications of the physical phenomena taking place.

Acknowledgements

First, I would like to thank my family for cheering me on through this, and all endeavors. Their observations that I always seem to be procrastinating my work and feigned interest in this highly specific study have helped keep me in check throughout the process. I would especially like to thank my fiance for his support from afar as well as occasional reviews of my work.

I would also like to thank my classmates, in particular Capt Joanna Williams, for serving as a sounding board and a sanity check throughout our time at AFIT. Long days of work and much needed study breaks would not have been the same without our senses of humor and our bonding through shared experiences.

Additionally, I would like to thank my advisor for his counseling over the last two years. I would also like to thank my committee for their enthusiasm for my work and setting aside time to assist and encourage me. I have learned a great deal under their instruction, both academically and practically.

Lastly, I would like to thank the High Altitude Observatory for hosting research activities at the Center Green facility. In particular, I would like to thank Sarah Gibson for her enthusiasm and coordination as well as K. D. Leka and Maria Kazachenko for their guidance and encouragement with my work.

Taylor R. Whitney

Table of Contents

List of Figures

Figure

Page

List of Tables

List of Abbreviations

AR active region

CCD charge-coupled device

CEA cylindrical equal area

CME coronal mass ejection

DoD Department of Defense

GOES Geostationary Operational Environmental Satellite

HAO High Altitude Observatory

HARP HMI Active Region Patch

HMI Helioseismic and Magnetic Imager

JSOC Joint Science Operations Center

LMSAL Lockheed Martin Solar and Astrophysics Laboratory

LoS line-of-sight

MDI Michelson Doppler Imager

NASA National Aeronautics and Space Administration

NOAA National Oceanic and Atmospheric Administration

SDO Solar Dynamics Observatory

SHARP SpaceWeather HMI Active Region Patch

SID Sudden Ionospheric Disturbance

SOHO Solar and Heliospheric Observatory

SWPC Space Weather Prediction Center

TAI International Atomic Time

UTC Coordinated Universal Time

I. Introduction

Solar flares cause disruptions to the electric and magnetic fields incident on the Earth from the Sun. In particular, this poses a danger to personnel and equipment, including Department of Defense (DoD) operations, in the space environment. Solar flares can cause disturbances within the Earth's atmosphere that can impact both natural and anthropogenic resources. Energetic particles from flares heat the atmosphere, causing it to expand and increase drag on satellites, which then forces them to expend more fuel in their orbit. Atmospheric changes as well as intensified emissions from flares can further result in degradation of satellite operations (Goddard Space Flight Center, 2020). In the ionosphere, solar flares cause Sudden Ionospheric Disturbances (SIDs), which lead to changes in electronic composition and to anomalies in signals from navigation systems and satellite communications (Liu et al., 2004; Qian et al., 2012). A study by Eastwood et al. (2017) estimates that a storm of similar level to the Carrington Event of 1859 could have an economic cost on the order of trillions of dollars in the United States alone.

Protection from these effects comes in the form of improved forecasting abilities to allow for a better reactive capability before the flare reaches the Earth or its spacecraft. Current forecasting techniques rely on climatological indications of the likelihood that a solar active region (AR) will produce a flare of a given strength. Improvements in flare forecasting can be made with greater understanding of the phenomena on the Sun that drive flare events, particularly magnetic reconnection. Simply put, magnetic reconnection is the rejoining of magnetic field lines that have been turbulently torn apart, as is done during a solar flare.

In plasma physics, the induction equation (Equation 1) describes the change in magnetic field lines through advection—the first term on the right hand side—and diffusion—the second term (Gurnett and Bhattacharjee, 2017; Priest, 2014):

$$\frac{\partial \vec{B}}{\partial t} = \nabla \times (\vec{u} \times \vec{B}) + \frac{1}{\mu_0 \sigma} \nabla^2 \vec{B} \tag{1}$$

According to Alfvén's theorem, the magnetic field lines are frozen into and move with the bulk plasma motion, such that the advection term dominates the induction equation and diffusion can be ignored. This requires that magnetic topologies are conserved, given that magnetic field lines cannot move with respect to the bulk plasma flow (Gurnett and Bhattacharjee, 2017).

Conversely, magnetic reconnection occurs in a diffusion-dominated region that violates Alfvén's theorem. Thus, the diffusion term in the induction equation must be considered. The violent flare process bursts open magnetic field lines and results in a configuration such as that in Figure 1 in which the opposing magnetic field regions are separated by a magnetically neutral surface. In this configuration, particles are rapidly accelerated out of the solar atmosphere and may be directed toward the Earth. After the event, decreased pressure at low solar altitudes causes field lines to drift toward the neutral point, where they reconnect. In doing so, plasma is transported across the magnetically neutral surface (Figure 1). The reconnection point moves up in altitude until equilibrium is reached. This results in a change in the flux in a closed loop, contradicting the flux conservation requirement of Alfvén's theorem (Gurnett and Bhattacharjee, 2017; Kopp and Pneuman, 1976; Priest, 2014).

Current magnetic reconnection models do not successfully predict the speeds at which the reconnections occur. The main model, the Sweet-Parker model, uses a steady diffusion layer over the entire boundary in which magnetic field lines enter at the same rate it diffuses outward. However, this produces a much slower speed than expected. For fast reconnection, adjustments are made to this model (Priest, 2014).

The Petschek model considers a diffusion region that is only a segment of the boundary and takes into account the flow external to the diffusion region (Priest,
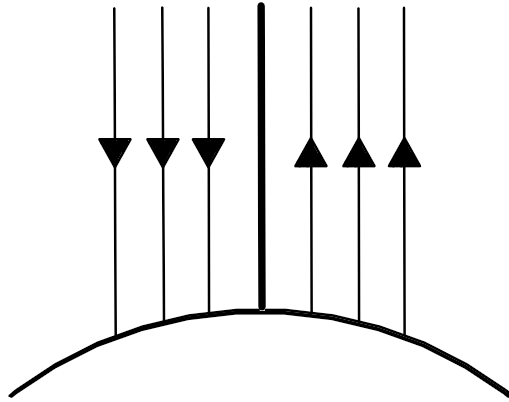
Figure 1. Magnetic field topology following a solar flare. Regions of opposing magnetic field are separated by a magnetically neutral surface, depicted by the thick black line.

2014). Resulting speeds are faster than the Sweet-Parker model and can even be used to accurately describe chromospheric reconnection (Chae et al., 2002). Fast reconnection has also been described using a flux pile-up method in which magnetic field lines get closer approaching the diffusion region. This type of reconnection produces a slow-mode expansion of the plasma and the central diffusion regions can be much larger than with the Petschek model (Priest, 2014). This type of model could account for discrepancies between photospheric reconnection signatures and the Sweet-Parker model, but should be used with caution, due to the length scales of turbulent diffusion and of magnetogram resolution in verification (Chae et al., 2008).

The actual reconnection event occurs higher in the solar atmosphere. However, the use of photospheric data can still help improve understanding of the upper solar atmosphere. Slow photospheric—and subphotospheric—motions drive the energy supply to an AR, both through the twisting and shearing of coronal magnetic structures and through the emergence of new current-carrying magnetic flux in the photosphere (Wheatland, 2008). Furthermore, photospheric observations have previously been used to create coronal magnetic field models (Scherrer et al., 2012).

3

II. Background

2.1 Previous Research

As the first decade of the Helioseismic and Magnetic Imager (HMI)—onboard the Solar Dynamics Observatory (SDO)—is only just concluding, studies analyzing the entirety of the dataset or a dataset of this size are relatively uncommon. This work serves to establish an analysis of this scale.

Furthermore, given that the main reconnection event associated with solar flares occurs higher in the solar atmosphere, studies using the magnetogram data for the investigation into magnetic reconnection are similarly uncommon. The idea for this study originated from a case study of Labor Day 2017 storms by Loper (2018). In this case study, three of the large flares that occurred between 4 and 10 September were combined into an epoch analysis. This epoch setup serves as the foundation for the epoch analyses created in this work (see Methodology). Magnetic field parameters studied include:

- Line-of-sight (LoS) area of active pixels

- Total unsigned flux

- Mean inclination angle

- Mean shear angle

- Mean photospheric excess magnetic energy density

- Mean current helicity.

Kazachenko et al. (2017) created a database of flare ribbons, which are enhancements in Hα and 1600 Å emissions and correspond to footprints of the newly

reconnected flux tubes. With this database, they analyzed flare ribbons associated with C1.0 and stronger flares that occurred within 45° of solar meridian between April 2010 and April 2016. When compared with flare peak x-ray flux, the reconnection flux (calculated as the unsigned magnetic flux spanned by the flare ribbon) has a much stronger correlation than the unsigned AR flux. This result suggests that there are magnetic properties that relate to the strength of a solar flare, but they are more easily seen when isolating the magnetic flux that is associated with the reconnection rather than the flux of the entire AR.

Bobra and Couvidat (2015) applied a machine-learning algorithm to M- and X-Class flares in order to forecast these events using HMI vector magnetic field data. They look at 303 ARs in which a flare occurred within 24 hours after a sample time and 5000 randomly selected ARs in which a flare did not occur within 48 hours after a sample time, positive and negative samples respectively. The inclusion of negative samples is necessary in training a machine learning algorithm to predict whether or not an AR will flare. Events range from May 2010 to May 2014 and are characterized by the same magnetic field parameters used in this study, with the addition of parameters characterizing the Lorentz force. Using performance metrics regarding the forecasting algorithm, this study determined that using four parameters with the highest feature score provides roughly the same true skill statistic as the top 13 parameters combined. These four parameters are:

- Total unsigned current helicity

- Total magnitude of the Lorentz force

- Total photospheric magnetic free energy density

- Total unsigned vertical current.

A study by Mason and Hoeksema (2010) performed a similar analysis to this

study but the data used were from the Michelson Doppler Imager (MDI), the predecessor to the HMI. In their study, the data taken were full-disk LoS magnetograms on a 96-minute cadence for 1075 ARs between 15 April 1996 and 31 December 2008 with B-Class and greater flares. For these events, four parameters were chosen based on previous studies:

- Total unsigned magnetic flux

- Primary inversion line length

- Effective separation (of the two bipolar regions of an AR)

- Gradient-weighted inversion-line length.

Calculation of the primary polarity inversion line, similarly done in Bobra and Couvidat (2015), identifies the region in which the polarity changes in the AR, where shearing and magnetic complexity are greatest. This study found that the gradient-weighted inversion-line length has the strongest association with flaring, but cannot produce real-time flare forecasts well. They did determine, however, that a superposed epoch analysis does have the ability to identify weak systematic responses in the data.

While these studies all focus on varying sets of parameters, their findings do indicate that there are relationships between photospheric magnetic fields and solar flares. Further, many of the results focus on stronger flares and either do not include or do not find significant results for smaller events. Although the larger flares usually have greater geo-effective conditions, expanding the study to a larger database can help to better determine the underlying physics taking place during solar flares and the associated photospheric magnetic fields.

2.2 HMI Data

The HMI has been operational onboard National Aeronautics and Space Administration (NASA)'s SDO since 1 May 2010. It is a joint project between Stanford University's Hansen Experimental Physics Laboratory, the Lockheed Martin Solar and Astrophysics Laboratory (LMSAL), the High Altitude Observatory (HAO), and an additional 21 institutions to better understand and predict geo-effective solar events (Scherrer et al., 2012). Data from the HMI can be obtained from the Joint Science Operations Center (JSOC) at Stanford University (JSOC, 2019b). For this study, SpaceWeather HMI Active Region Patch (SHARP) data are acquired using the Python notebook created by Glogowski and Bobra (2016). Instrument description and calibration as well as data handling and scientific analysis can be found in Schou et al. (2012).

As an enhancement to the MDI instrument on the Solar and Heliospheric Observatory (SOHO), the HMI provides full-disk vector-field data at a high cadence. The instrument's science goals include the observation of dynamics in the convective zone as well as the solar dynamo, the origin and evolution of solar activity features, the sources and drivers of magnetic features, links in the corona and heliosphere between internal processes and dynamics, and precursors of disturbances for the improvement of space-weather forecasts (Scherrer et al., 2012). It is the first instrument that continuously maps vector magnetic fields from space on the full solar disk (Bobra and Couvidat, 2015). This study will focus on the photospheric observations of ARs, providing analysis of magnetic parameter changes during flare events.

2.2.1 HARPs

The HMI produces photospheric full-disk LoS magnetogram images. Using these and intensity images on the same cadence, HMI Active Region Patches (HARPs)

are automatically identified and tracked as the region moves across the solar disk on a 720-second (12-minute) cadence. The dataset serves to track enduring, coherent magnetic structures as they traverse the Earth-facing hemisphere of the Sun (Hoeksema et al., 2014; JSOC, 2019a). The ARs are given HARP numbers as identification. HARP numbers differ from National Oceanic and Atmospheric Administration (NOAA) AR numbers and may even be associated with multiple NOAA ARs, but each HARP file contains both types of identification. HARPs are identified by (Hoeksema et al., 2014):

- Identifying magnetically active pixels, those with an absolute LoS field greater than 100 Gauss

- Grouping active pixels into instantaneous activity patches, taking into account spherical geometry

    – These patches generally have smooth contours but may consist of several regions separated by quiet Sun

- Stringing together image-to-image associations with a latitude-dependent motion model to combine the instantaneous patches into a temporal track

    – Gaps exceeding 2 days result in separate HARPs.

Each HARP contains the time index of all associated instantaneous patches as well as geometric metadata and selected summary statistics of the active region. The instantaneous patches are coded as bitmaps of the rectangular bounding box in the charge-coupled device (CCD) plane. These bitmaps identify pixels as one of four types (JSOC, 2019c):

- Quiet pixels outside of the active region

- Active pixels outside of the active region

- Quiet pixels inside the active region

- Active pixels inside the active region.

2.2.2 SHARPs

In addition to the HARP data series, the JSOC produces a data series called SHARP that includes summary parameters of the HARPs (JSOC, 2019a). Each SHARP includes 31 maps of the active patch for every time step (again, a 12-minute cadence) with disambiguated field and thermodynamic parameters as well as uncertainties and errors thereof. These parameters are determined in the spectral line inversion that is used to interpret the spectro-polarimetric data. There is additionally a series of cylindrical equal area (CEA) data that includes 11 maps that are remapped to CEA heliographic coordinates centered on the HARP center point (Hoeksema et al., 2014). For the purposes of this study, the CEA data series was not used in favor of the greater breadth of information provided in the standard SHARP data series.

SHARP parameters are calculated for pixels that are within the active region and have a high confidence in the disambiguation. The disambiguation serves to resolve the 180° ambiguity that results from the inversion of the Zeeman splitting caused by the magnetic field lines (Hoeksema et al., 2014). The SHARP parameters, descriptions, and formulas are identified in Table 1.

2.3 Solar Flare Data

The Space Weather Prediction Center (SWPC) at NOAA maintains an archive of solar events (SWPC, 2019). These are automatically identified by Geostationary Operational Environmental Satellite (GOES) spacecraft using a detection algorithm and supplemented by forecaster input as needed. The algorithm compares current data to previous observations, up to three minutes prior, to determine the slope of

Table 1. SHARP parameters, descriptions, and calculations (Adapted from Bobra et al., 2014; Hoeksema et al., 2014; JSOC, 2019a, 2019c)

Keyword	Description	Unit	Formula
AREA_ACR	De-projected area of active pixels	μH	$A_{total} = \sum dA$
USFLUX	Total unsigned flux	$Maxwells$	$\phi = \sum \lvert B_z \rvert dA$
MEANGAM	Mean inclination angle	$Degrees$	$\bar{\gamma} = \frac{1}{N} \sum \tan^{-1}\left(\frac{B_h}{B_z}\right)$
MEANGBT	Mean value of the total field gradient	G/Mm	$\overline{\lvert \nabla B_{tot} \rvert} = \frac{1}{N} \sum \sqrt{\left(\frac{\partial B}{\partial x}\right)^2 + \left(\frac{\partial B}{\partial y}\right)^2}$
MEANGBZ	Mean value of the vertical field gradient	G/Mm	$\overline{\lvert \nabla B_z \rvert} = \frac{1}{N} \sum \sqrt{\left(\frac{\partial B_z}{\partial x}\right)^2 + \left(\frac{\partial B_z}{\partial y}\right)^2}$
MEANGBH	Mean value of the horizontal field gradient	G/Mm	$\overline{\lvert \nabla B_h \rvert} = \frac{1}{N} \sum \sqrt{\left(\frac{\partial B_h}{\partial x}\right)^2 + \left(\frac{\partial B_h}{\partial y}\right)^2}$
MEANJZD	Mean vertical current density	mA/m^2	$J_z \propto \frac{1}{N} \sum \left(\frac{\partial B_y}{\partial x} - \frac{\partial B_x}{\partial y}\right)$
TOTUSJZ	Total unsigned vertical current	A	$J_{z_{total}} = \sum \lvert J_z \rvert dA$
MEANALP	Characteristic twist parameter, α	$1/Mm$	$\alpha_{total} \propto \frac{\sum J_z B_z}{\sum B_z^2}$
MEANJZH	Mean current helicity	G^2/m	$\bar{H}_c \propto \frac{1}{N} \sum B_z J_z$
TOTUSJH	Total unsigned current helicity	G^2/m	$H_{c_{total}} \propto \sum \lvert B_z J_z \rvert$
ABSNJZH	Absolute value of the net current helicity	G^2/m	$H_{c_{abs}} \propto \left\lvert \sum B_z J_z \right\rvert$
SAVNCPP	Sum of the absolute value of the net currents per polarity	A	$J_{z_{sum}} \propto \left\lvert \sum^{B_z^+} J_z dA \right\rvert + \left\lvert \sum^{B_z^-} J_z dA \right\rvert$
MEANPOT	Mean photospheric excess magnetic energy density	erg/cm^3	$\bar{\rho} \propto \frac{1}{N} \sum (\vec{B}^{Obs} - \vec{B}^{Pot})^2$
TOTPOT	Total photospheric magnetic energy density	erg/cm	$\rho_{total} \propto \sum (\vec{B}^{Obs} - \vec{B}^{Pot})^2 dA$
MEANSHR	Mean shear angle	$Degrees$	$\bar{\Gamma} = \frac{1}{N} \sum \cos^{-1}\left(\frac{\vec{B}^{Obs} \cdot \vec{B}^{Pot}}{B^{Obs} B^{Pot}}\right)$
SHRGT45	Percentage of pixels with a mean shear angle greater than 45°	$Percent$	$\frac{area\ with\ shear > 45°}{HARP\ area}$

the x-ray flux and changes therein. From there, the algorithm determines whether the event is at the beginning, maximum, or end and notes the times and maximum x-ray flux in addition to various other parameters not used in this study (SWPC, 2009). Event ends are considered to be when the flux level reaches its half-max height, respective to the pre-flare background level (SWPC, 2009, 2019). Associated NOAA AR numbers are assigned by the observatory or SWPC staff, depending on the event type (SWPC, 2019).

Among the solar events identified using SWPC's algorithm are solar flares. Available to the public from SWPC (2019), these archives can be downloaded in the form of yearly compressed and zipped (*.tar.gz) files that contain daily summaries. Flare dates and times are all given in Coordinated Universal Time (UTC). This time scale differs from that of the SHARP data, which are in International Atomic Time (TAI). However, UTC is derived from TAI and only differs by 37 seconds (International Bureau of Weights and Measures, 2019a, 2019b), which is about 5% of the HMI observation frequency. Therefore, the difference in time scales is ignored for the purposes of this study.

Once all the files were acquired for 2010 through September 2019, a simple code interpreted the data. With the individual files as an input, the code sifted through the information to isolate only the events classified as x-ray flares. The associated start time, flare strength, and NOAA AR were output into a *.csv file to be easily accessed by the analysis code (see Methodology). Start times were used preferentially over maximum times as the imagery would have been impacted at the maximum time with the flare already in progress. Furthermore, the time between beginning and maximum of a flare varies for each event. As a result, the data leading up to flare maximum cannot be accurately categorized as part of the flare itself or as part of the lead-up for a dataset of this size (Gibson et al., 2019).

2.3.1 Flare Statistics

The first entry in the HARP dataset is dated 1 May 2010. Data were collected through September 2019, but the last HARP recorded in this time ends on 4 September 2019. In this dataset, there were 13,508 flares recorded. Of these flares, 5,493 were B-Class, 7,210 were C-Class, 697 were M-Class, and 46 were X-Class. The remainder were A-Class and unused in this study. The distribution of flare strengths peaks strongly at C1.2, of which there are 519 flares, as seen in Figure 2. As in the study by Wheatland (2008), there is a power-law distribution of flare strengths.

Due to the logarithmic scale of flare classes, the bin size increases for each successive category. B-Class flares have strengths ranging from $1 \times 10^{-7}\ W/m^2$ to $1 \times 10^{-6}\ W/m^2$, C-Class flares have strengths of $1 \times 10^{-6} - 1 \times 10^{-5}\ W/m^2$, M-Class flares have strengths $1 \times 10^{-5} - 1 \times 10^{-4}\ W/m^2$, and X-Class flares have strengths $1 \times 10^{-4}\ W/m^2$ and greater. These ranges are further separated into sub-classes by magnitude of the x-ray flux. Each stronger class has a larger bin size (e.g. the change in flux from B1 to B2 compared to the change in flux from C1 to C2) by a factor of ten and thus has a wider range of flares counted. As a result, there is a discontinuity between each class in the distribution of flare strengths, seen in Figure 2.

The B-Class flares do not appear to follow the same distribution. B-Class flares are more easily washed out by stronger or a high frequency of flares (Gibson et al., 2019) or by the background x-ray flux during solar max. For example, in a HARP in March 2019 (HARP 7350), there were so many flares that the background flux levels were never able to return to normal (Figure 3). Similarly, this phenomenon is commonly observed in ARs that produce strong flares, such as in HARP 7115 in Figure 4. For events such as these, any B-Class flares would not be identified by the SWPC detection algorithm. As a result, especially near solar maximum, the B-Class flares that are recorded do not represent the greater number that actually occur.
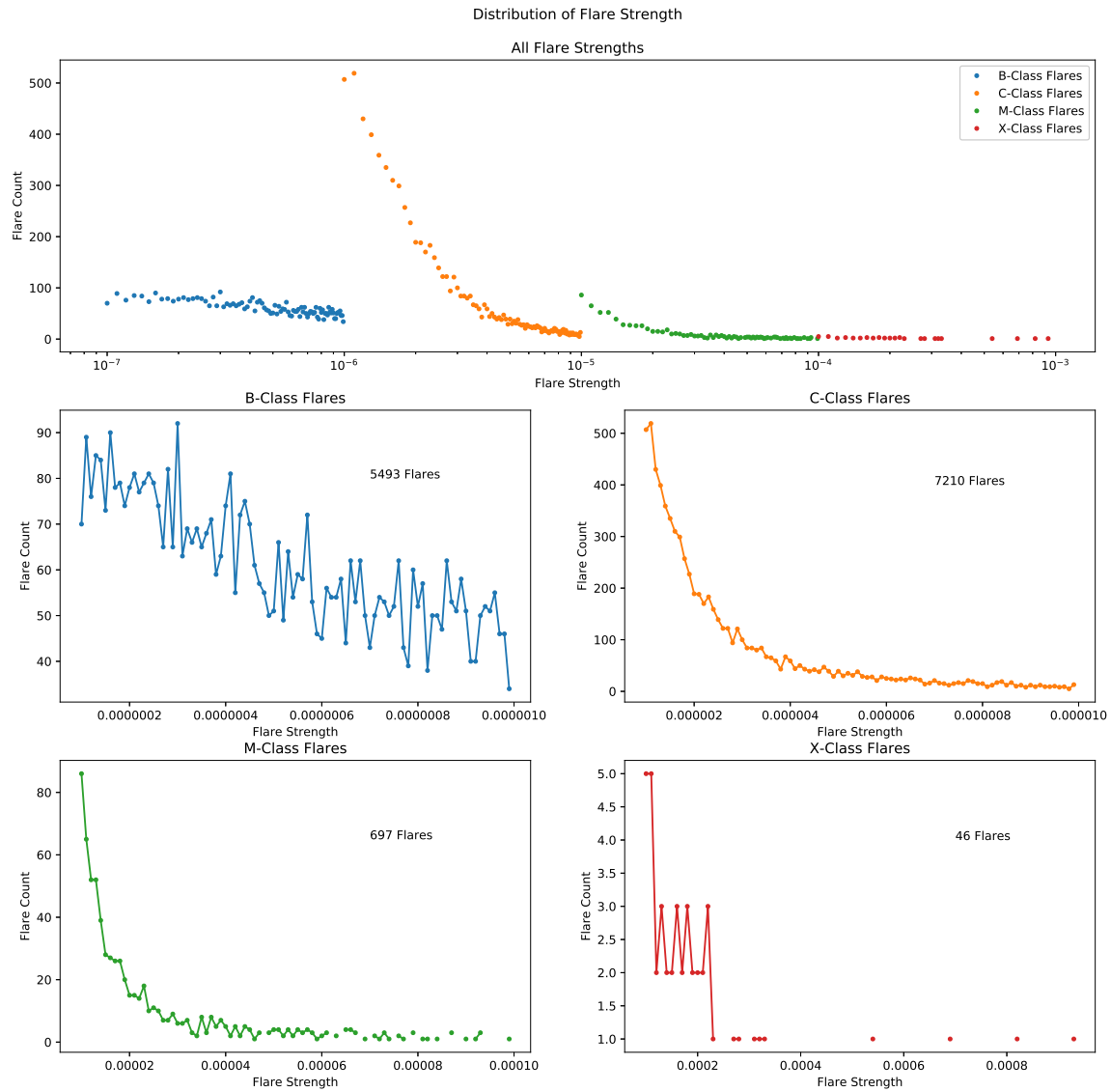
Figure 2. Distribution of flare strength in the dataset spanning May 2010 – September 2019. The top plot is a semi-logarithmic plot in the x-axis to match the scale for flare classification. The bottom four plots show individual distributions of each flare class. The strength distribution peaks at C1.2 with 519 flares. Flare strengths are identified by SWPC (2019).
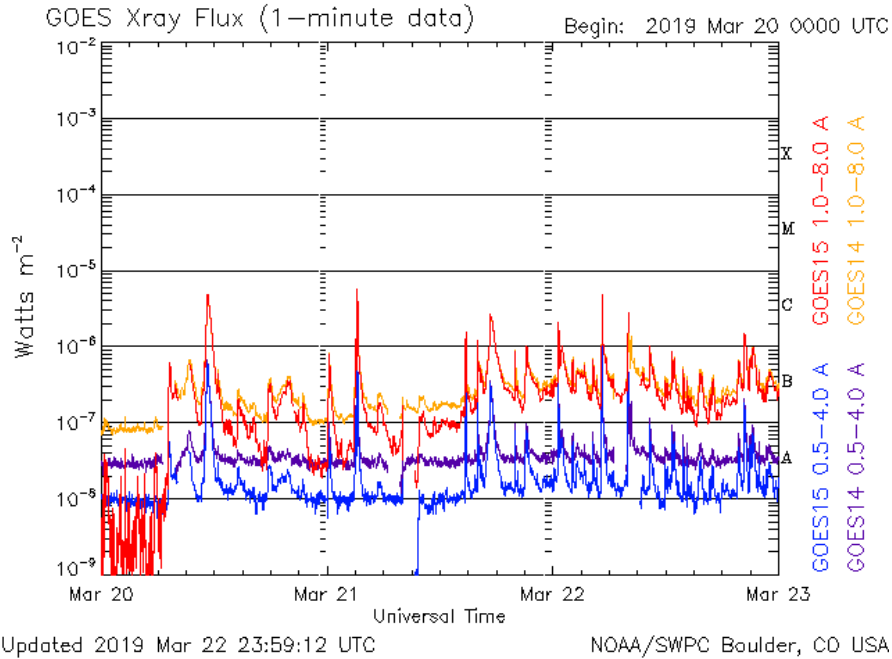
Figure 3. X-ray flux for the series of flares beginning on 20 March 2019. The active region had multiple C-Class flares in quick succession, preventing the background x-ray flux from returning to normal levels between flares. Image courtesy of NOAA SWPC (NOAA, 2019).
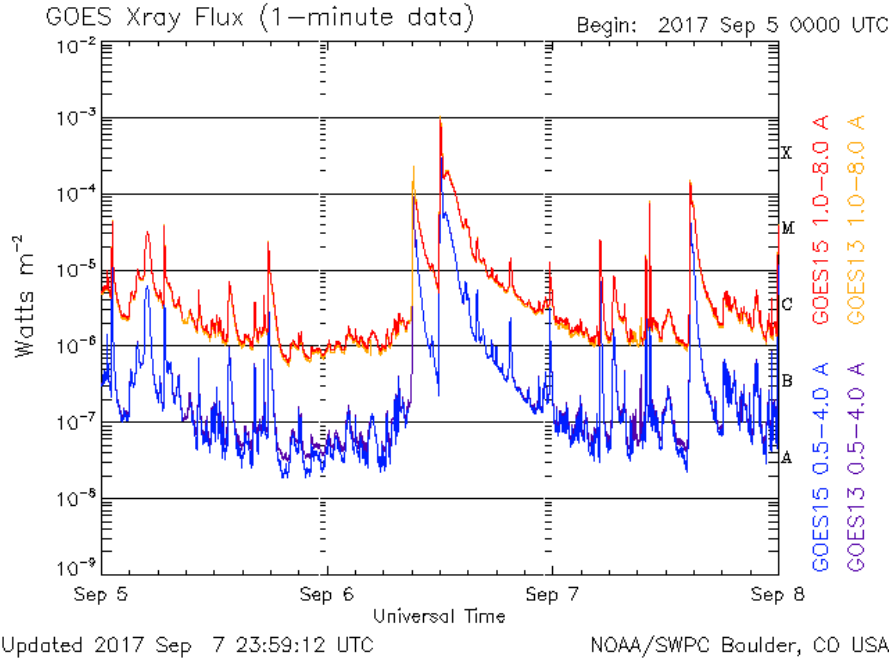

Figure 4. X-ray flux for the Labor Day storms of 2017, including the X9.3 flare on 6 September 2017. The extreme nature of the flares during this storming event raised the overall x-ray flux levels for multiple days before and after. Image courtesy of NOAA SWPC (NOAA, 2019).

14

III. Methodology

3.1 Small Flare Case Study

Initially, a subset of flares was considered as a case study of small flares. Four flares were selected to compare six summary SHARP parameters in an epoch analysis. These parameters were:

- Area of active pixels

- Total unsigned flux

- Mean inclination angle

- Mean shear angle

- Mean photospheric excess magnetic energy density

- Mean current helicity.

Descriptions of SHARP parameters can be found in Table 1. The initial case study was modeled after that of Loper (2018), using one of the same X-Class flares as a comparison to three smaller flares. Data for two hours prior to and four hours following flares were combined into epoch analyses in order to assess any trends that could aid in the forecasting of solar flares.

Four events were chosen that were the beginning of or isolated storming events. Furthermore, three of the events were specifically chosen to be smaller flares as a means of comparing the smaller events to each other as well as to a stronger flare. As stronger flares tend to be of greater emphasis in studies, little is yet known about the trends associated with smaller, more frequent flares.

3.1.1 6 September 2017

Despite its proximity to the minimum of solar cycle 24, the active region of 28 August - 10 September 2017 produced multiple strong solar flares. The strongest of these was an X9.3 flare—the strongest flare of the solar cycle—that occurred on 6 September at 12:02 UTC and will be used in this study (Figures 4 and 5). A precursory X2.2 flare appears to have provided the necessary set-up for the larger X9.3 flare that occurred approximately three hours after (Verma, 2018). These flares were part of HARP 7115 and NOAA AR 12673, for which HARP data covers 28 August at 09:00 UTC through 10 September at 11:12 UTC. The active region crossed the meridian on 3 September at 20:12 UTC (JSOC, 2019b). The flare occurred shortly after the active region had crossed the meridian, which means that the data will not be greatly skewed by the difference between the LoS from HMI and the radial direction on the Sun.
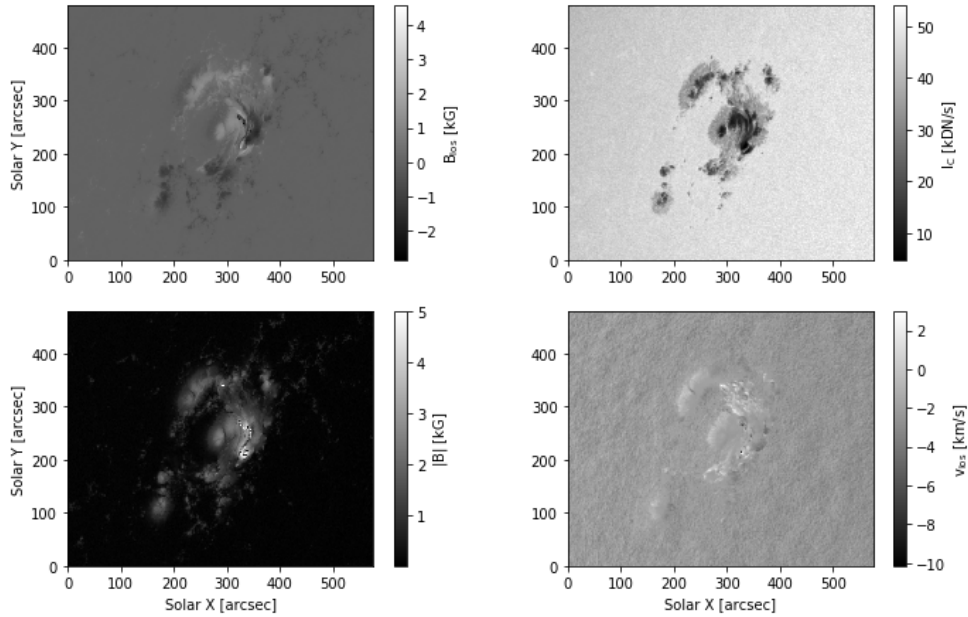

Figure 5. SDO magnetogram (upper left), continuum intensity (upper right), magnetic field strength (bottom left), and Dopplergram (bottom right) images of HARP 7115 (NOAA 12673) from 2 minutes prior to the X9.3 flare on 6 September 2017. Figure generated with data from JSOC (2019b) acquired using the Python notebook created by Glogowski and Bobra (2016).

3.1.2 20 March 2019

While the active region of 15 - 25 March 2019 only produced a maximum C5.3 flare, its background x-ray flux level was raised into the B-class flare level (Figure 3). From this active region, the initial flare at 07:14 UTC, with a strength of B6.1 (Figure 6), and the first C-Class flare at 11:18 UTC, with a strength of C4.8 (Figure 7), will be considered. As with the X-Class flares of 2017, the initial weaker flare appears to be a triggering mechanism for the subsequent storming events. These flares come from HARP 7350—NOAA AR 12736—which has HARP data from 15 March at 21:24 UTC through 25 March at 04:36 UTC. The active region crossed the meridian on 18 March at 16:48 UTC (JSOC, 2019b). Similar to the 6 September 2017 storms, both flares occurred shortly after the active region crossed the meridian.

3.1.3 30 March 2018

The active region of 29 March - 7 April 2018 produced one C-class flare followed by a few smaller flares. In contrast to the 20 March 2019 solar flares, the background x-ray flux levels are not elevated (Figure 8). On 30 March 2018, this active region produced a C4.6 flare at 08:04 UTC (Figure 9), which will be considered for this study. Similar to the other HARPs, the flare has a small preceding flare that occurred less than three hours before. However, this flare is more isolated following the event than the others considered. This flare is part of HARP 7246 and NOAA AR 12703. HARP data begins on 29 March at 13:12 UTC and ends on 7 April 03:00 UTC, crossing the meridian on 4 April at 21:00 UTC (JSOC, 2019b). Unlike the two previous active regions, this flare occurred shortly after the active region appeared on the eastern limb, affecting the sunspot geometry given the large deviation of HMI's LoS from radial.
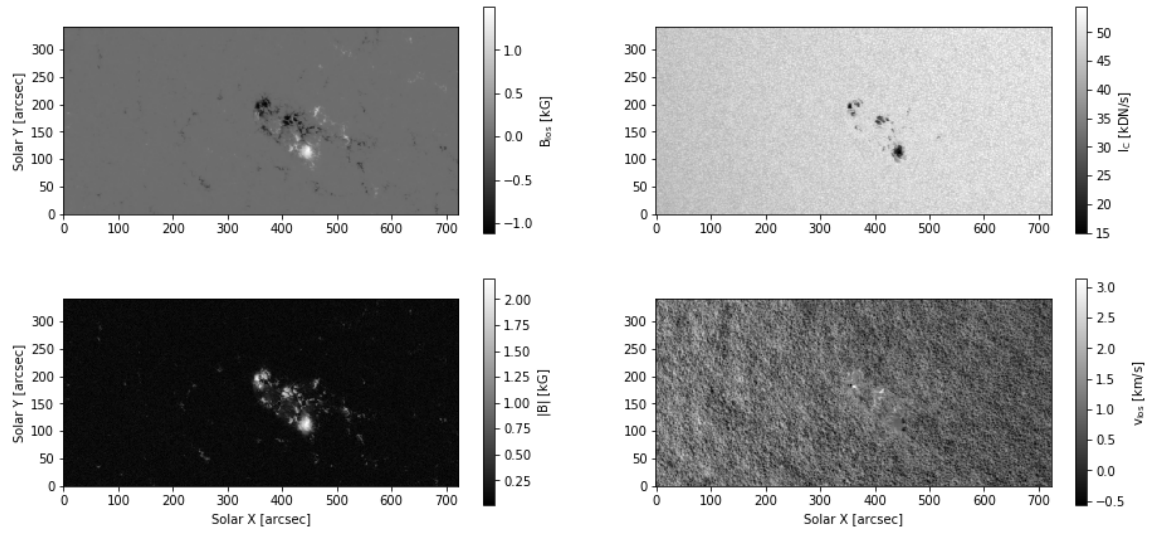
Figure 6. SDO magnetogram (upper left), continuum intensity (upper right), magnetic field strength (bottom left), and Dopplergram (bottom right) images of HARP 7350 (NOAA 12736) from 2 minutes prior to the B6.1 flare on 20 March 2019. Figure generated with data from JSOC (2019b) acquired using the Python notebook created by Glogowski and Bobra (2016).

Figure 7. SDO magnetogram (upper left), continuum intensity (upper right), magnetic field strength (bottom left), and Dopplergram (bottom right) images of HARP 7350 (NOAA 12736) from 6 minutes prior to the C4.8 flare on 20 March 2019. Figure generated with data from JSOC (2019b) acquired using the Python notebook created by Glogowski and Bobra (2016).

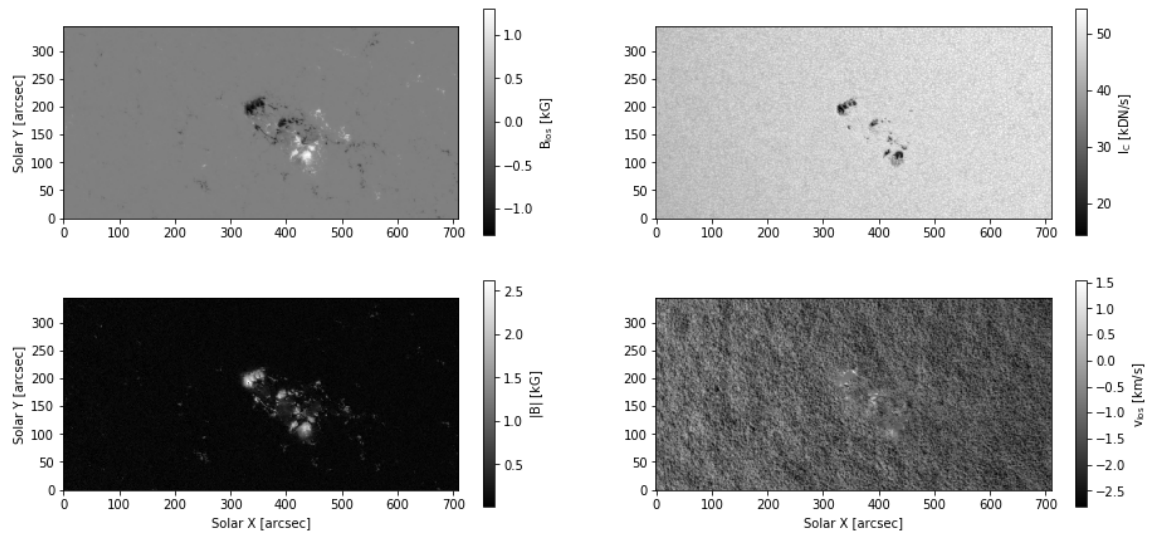**Figure 8. X-ray flux for the C4.6 flare on 30 March 2018. Image courtesy of NOAA SWPC (NOAA, 2019).**

Figure 9. SDO magnetogram (upper left), continuum intensity (upper right), magnetic field strength (bottom left), and Dopplergram (bottom right) images of HARP 7246 (NOAA 12703) from 4 minutes prior to the C4.6 flare on 30 March 2018. Figure generated with data from JSOC (2019b) acquired using the Python notebook created by Glogowski and Bobra (2016).
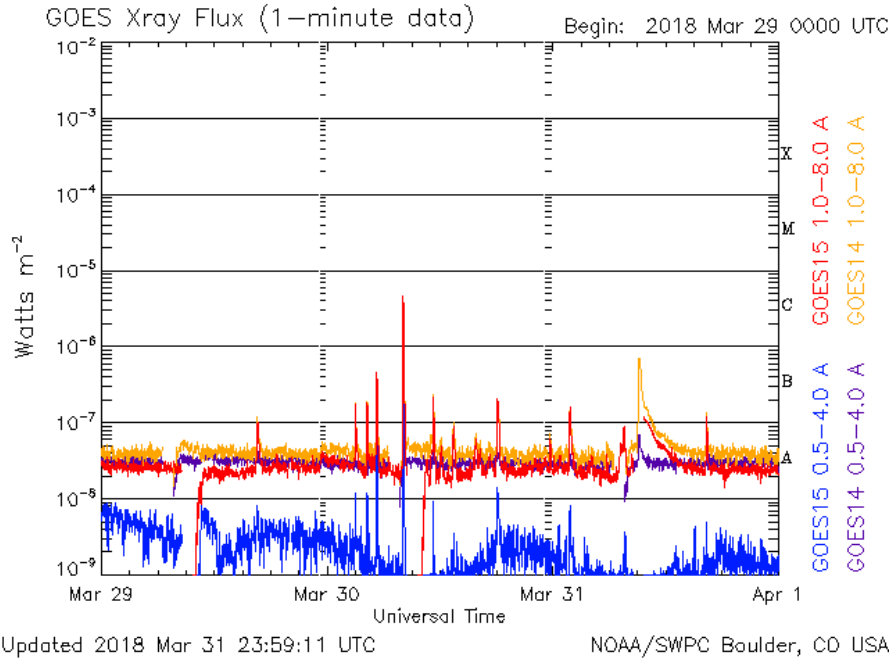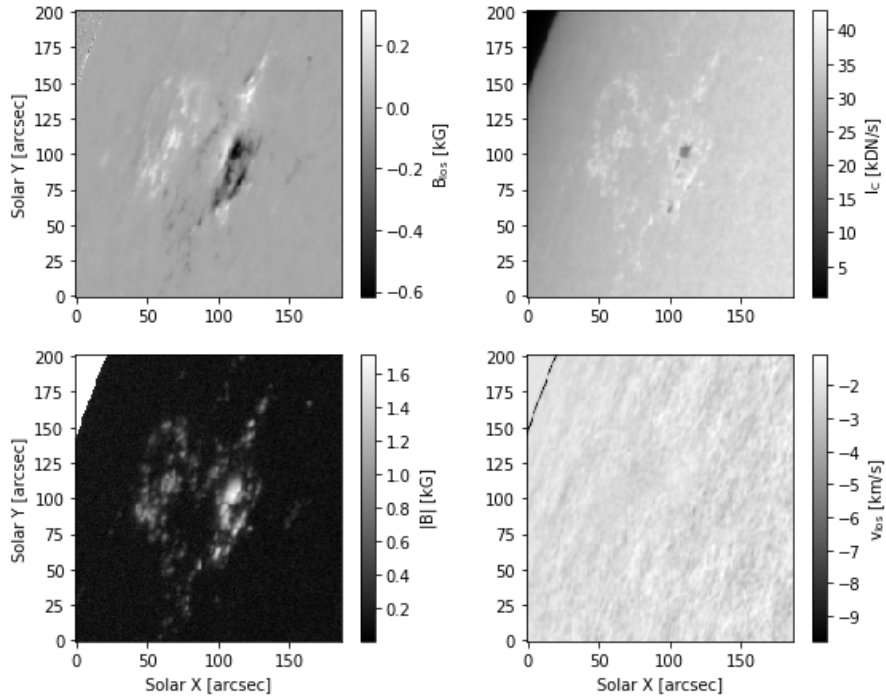
3.1.4 Case Study Results

In the epoch analysis, data are normalized to the value at the flare time and all times were adjusted to set the flare times to 12:00. This time was chosen arbitrarily to align all the flares when plotting. The flare times were considered the observation made closest to the maximum of the flare. This is adjusted for the expanded study to consider flare times as the observation closest to the start of the flare, as discussed in the Background section. Results can be found in Figure 10. Because the two flares on 20 March 2019 are approximately four hours apart, the final two hours of the B-Class flare will overlap with the initial two hours of the C-Class flare.

For this small collection of events, the trends found among the smaller flares often differ from the trends seen in the stronger flare. This study did only compare a single X-Class flare and may not represent the characteristics of all X-Class flares. However, among the smaller flares, there do appear to be similarities prior to the event:

- Increasing size of the activity within the HARP within the hour before

- Increasing unsigned flux in the entire two hours considered

- Local minima in current helicity, indicating untwisting of the magnetic field lines, a trend shared by the X-Class flare.

There are additionally similar trends among the smaller flares following the events, such as increases in area of active pixels and total unsigned flux, a spike in inclination angle within an hour, overall decrease in mean shear angle, and perhaps increases in both mean photospheric excess magnetic energy density and mean current helicity. After these smaller flares, the HARPs continue to grow and increase their magnetic complexity.
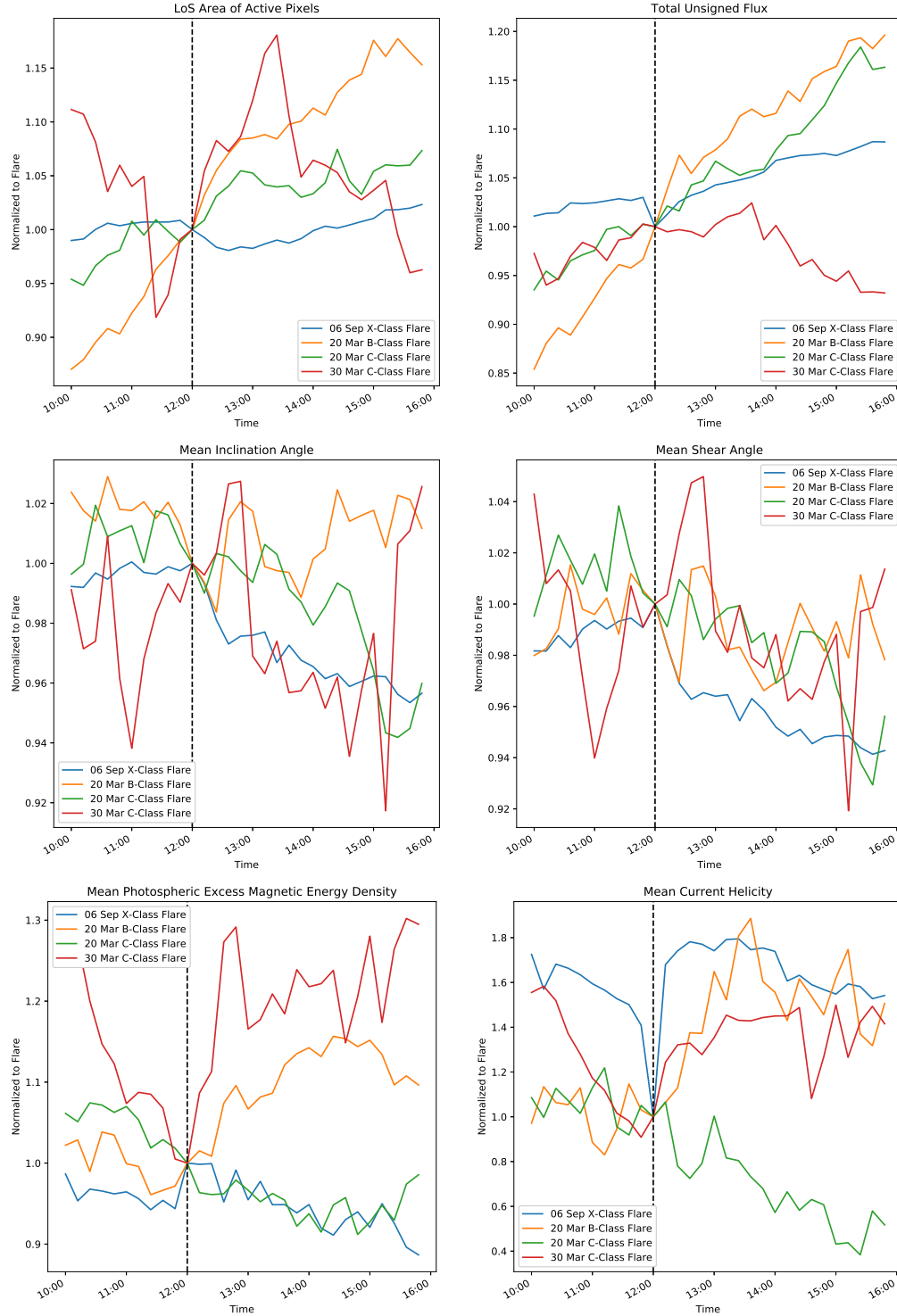
Figure 10. Area of active pixels, total unsigned flux, mean inclination angle, mean shear angle, mean photospheric excess magnetic energy density, and mean current helicity for four solar flares between 2017 and 2019. All data are normalized to the value at the flare time and times were adjusted to set all flare times to 1200. Plots generated with data from JSOC (2019b) acquired using the Python notebook created by Glogowski and Bobra (2016).

21

3.2 HMI Dataset

After completion of the initial case study, the same idea was applied to analysis of nearly a decade of HMI data, collected at the end of September 2019. The goal of this expanded study was to assess statistically more significant trends, rather than a few events to represent this larger dataset. In addition to a greater sample size of events, the study was also extended to include all of the available SHARP parameters—listed in Table 1. This dataset, spanning the time between May 2010 and September 2019, includes nearly the entirety of solar cycle 24. It begins shortly after the minimum of solar cycle 24 and includes its maximum and initial transition to solar cycle 25.

The increased size of the dataset calls for automation of the entire process. For both the flare database (SWPC, 2019) and the HARP information (JSOC, 2019b), data through the end of September 2019 were downloaded into *.csv files. This provided easier access to the data than downloading the same information each time the code ran. HARP data for the entirety of the time period was downladed, regardless of whether or not there was a flare associated with each HARP. The archive contains data for multiple types of solar events (SWPC, 2019). Thus, the process of downloading data also included a step to retrieve only the solar flare data.

With both sets of data, the times were converted to `datetime` format and flare start times were associated with the nearest HARP time. In addition, a time array was created with necessary entries for the epoch analysis (10:00 to 16:00 so that the flares would all be plotted to start at 12:00). Next, the data for two hours prior to and four hours following a flare were extracted and normalized to the value at the flare start time for all SHARP parameters. Finally, the isolated epoch flare data was parsed to eliminate outlier events. This was done separately for all flares as well as for subsets of each flare class.

3.3 Statistical Analysis

3.3.1 Eliminating Outliers

For plotting the epoch analyses of the dataset, two masks were applied to remove outliers. Masks were applied separately for each compilation of epoch data—for the full dataset as well as the flare class subsets. The first mask was to eliminate flares outside of three standard deviations from the average value. Flares were discarded if any parameter at any time step in the six-hour epoch window was outside of the standard deviation limits. When included, these flares dominated the dataset, falsely skewing the results. Standard deviation limits applied for each parameter, normalized to the flare time values, can be found in Figure 11.

Next, flares outside of 70° longitude were eliminated. Longitudinal masks serve to eliminate data in which the LoS magnetic fields measured by the HMI are falsely dominated by horizontal rather than radial magnetic fields as well as data impacted by apparent solar limb effects. Limb darkening results from the variation of the depth surveyed in an image due to the optical depth of the plasma and the geometry of the LoS, affecting all pixels at a given radius. Foreshortening affects only the sunspots, but results in a distortion of the spot near the limb as the LoS looks across the sunspot rather than directly onto it.

Studies of solar events, such as Kazachenko et al. (2017) and Bobra and Couvidat (2015), include similar limits to their data. In the study by Kazachenko et al. (2017), a limit of 45° longitude was applied. This was to exclude magnetic field data that were more transverse than radial, with respect to LoS. Meanwhile, Bobra and Couvidat (2015) apply a mask of 70° from central meridian as the signal-to-noise ratio in the SHARP parameters significantly increases beyond this longitude (Bobra et al., 2014). In a study by Criscuoli et al. (2017) regarding network and faculae from
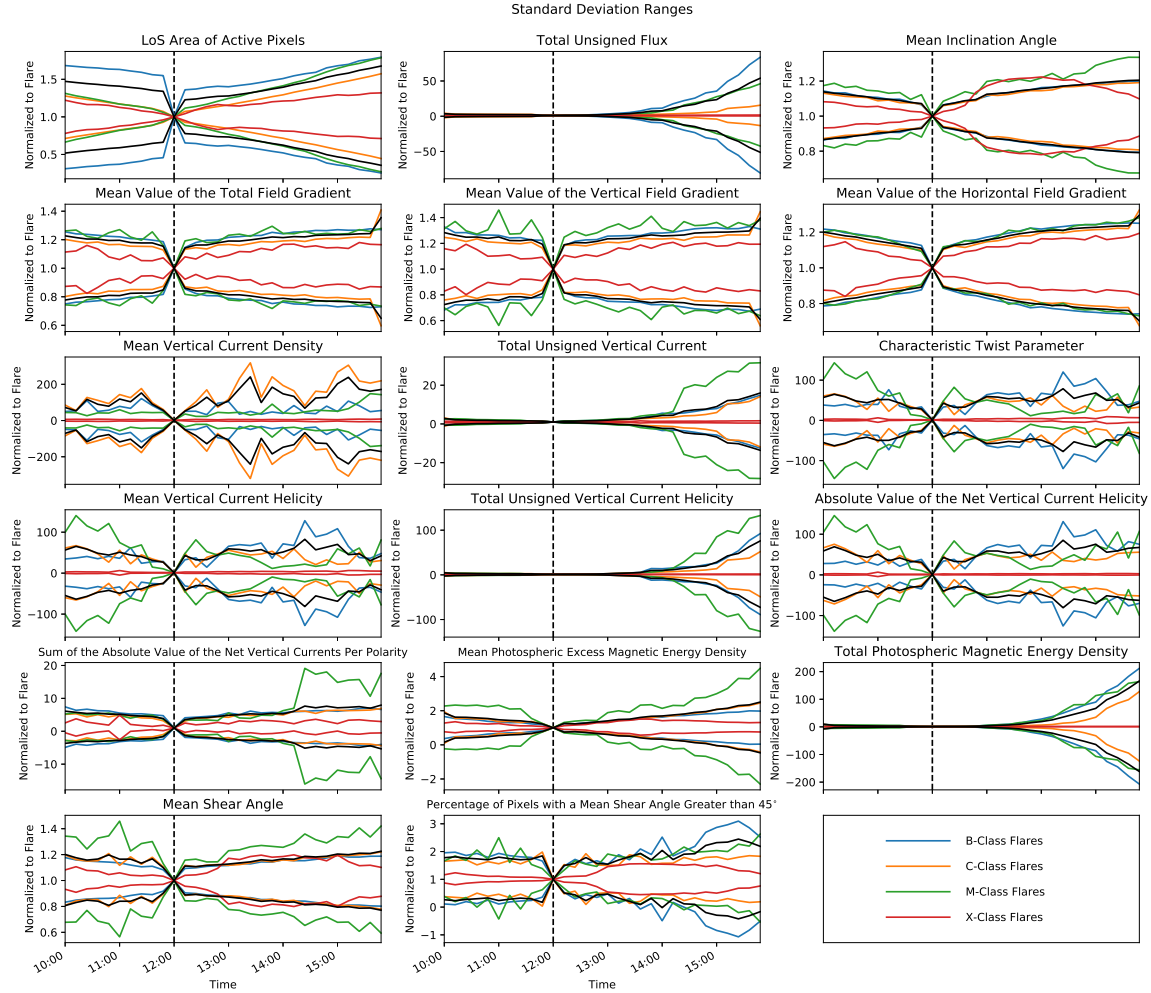
Figure 11. Standard deviation limits applied to the dataset and subsets for this study. Data outside these limits are disregarded for this study. Plotted lines represent three standard deviations from the average values of a given subset. Each color represents a different subset: all flares in black, B-Class flares in blue, C-Class flares in orange, M-Class flares in green, and X-Class flares in red. Values are normalized to flare start times, denoted by the vertical dashed line. SHARP data are acquired from JSOC using the Python notebook created by Glogowski and Bobra (2016) and flare times are identified by SWPC (2019).

24

the same dataset, observations are included as far out as 78° but a deconvolution is performed to compensate for the scattered light effects near the solar limb. The remainder of the solar limb is disregarded only due to uncertainties in this region.

To determine the longitude mask best suited for this study, sets of plots were created with 45° and 70° masks as well as no mask. Comparison of these plots showed no significant differences between the masks, with fluctuations within a few percent. This indicates that the SHARP calculations do make corrections for longitude in the Stokes parameters. This correction is necessary in the HARP dataset as it tracks ARs to the limbs in order to maintain HARP history across the Earth-facing solar hemisphere (JSOC, 2019a). The dataset considered in this study represents this property of the HARP tracking algorithm as the greatest AR longitude included was 90.37°. The greatest longitude of of a flare included was 89.76°. However, flares along the limb can still be missed, as was the case with an X8.2 flare on 10 September 2017 (Loper, 2018). The 70° mask was used for this study in order to avoid lost or incomplete patches as they rotate onto and off the solar disk as well as to avoid some of the more extreme limb effects to the data.

Plots of all flares included in the analysis can be found in Appendix A. Distributions of flare classes that meet these considerations and are used in this study are found in Table 2. Again, the dataset is dominated significantly by weak C-Class flares, so much so that the C1 and C2 flares comprise 40% of the events considered. Further, despite the undersampling of B-Class flares, they still make up a larger portion of the dataset than either the M- or X-Class flares. Moreover, flares with a strength of X4 and greater are outside the limits of the applied masks. Prior to the masks, there were only four flares in this range: an X5.4, an X6.9, an X8.2, and an X9.3. The X6.9 and X8.2 flares were too close to the solar limb and the other two were beyond standard deviation limits, overpowering the general X-Class flare behavior.

Table 2. Distribution of flare strengths after removal of outlier events

Flare Class	Number of Flares Considered	Comparison to Unmasked Subset	Comparison to Total Considered
B	**2063**	**37.6%**	**37.2%**
B1	164	20.6%	2.9%
B2	225	29.6%	4.1%
B3	228	33.3%	4.1%
B4	258	39.7%	4.6%
B5	240	42.0%	4.3%
B6	266	49.4%	4.8%
B7	226	44.7%	4.1%
B8	246	47.5%	4.4%
B9	210	45.2%	3.8%
C	**3181**	**44.1%**	**57.3%**
C1	1528	42.0%	27.5%
C2	695	46.7%	12.5%
C3	348	47.5%	6.3%
C4	192	44.7%	3.5%
C5	139	45.4%	2.5%
C6	91	41.6%	1.6%
C7	83	50.0%	1.5%
C8	54	41.2%	1.0%
C9	51	53.1%	0.9%
M	**292**	**41.9%**	**5.3%**
M1	172	40.9%	3.1%
M2	49	42.2%	0.9%
M3	24	43.6%	0.4%
M4	17	56.7%	0.3%
M5	12	38.7%	0.2%
M6	7	36.8%	0.1%
M7	6	46.2%	0.1%
M8	3	50.0%	0.05%
M9	2	33.3%	0.04%
X	**15**	**32.6%**	**0.3%**
X1	11	37.9%	0.2%
X2	3	30.0%	0.05%
X3	1	33.3%	0.02%
X4	0	0%	0%
X5	0	0%	0%
X6	0	0%	0%
X7	0	0%	0%
X8	0	0%	0%
X9	0	0%	0%
Total	**5551**	**41.1%**	**100%**

3.3.2 Displaying Data

In order to compare the events, all parameters were normalized to the value of each flare at its start time. This allows all the events to be displayed on the same scale and shows the changes relative to the flare onset. While the flare maximum time is used to determine flare strength and is typically the time associated with the event, the start time was used instead to avoid contamination of the data from the ongoing flare (see Background).

Due to the substantial quantity of flares in the dataset, displaying them all on a single plot, as in Appendix A, gives a crowded plot on which it is difficult to determine any trends. To summarize the dataset, averages and medians of the data for each point in time across all flares of a given strength were plotted. Median plots are used in this study and can be found in the Analysis and Results section. Average plots were not used but are included in Appendix B for comparison. Medians were chosen over averages since the data follow a power law distribution in which averages are more susceptible to outliers and may not provide an adequate representation.

3.4 Limitations

This study only considers flares that have an associated NOAA AR. The association is performed during the SHARP analysis and can be accessed through the header of the data file in the same manner as the SHARP parameters used in this study. Of the 13,508 flares that occurred between May 2010 and September 2019, 2,890 did not have an associated NOAA AR; this is approximately 21% of the dataset.

In the SWPC archive of solar events, there are seven occasions when the maximum time of the flare was missing, denoted as "////." For all of these events, the begin times were around or after 23:40 and the end times were around or before 00:05 the next day. In these instances, the maximum times were set to 00:00.

As previously mentioned, magnetic reconnection occurs in the solar atmosphere while the observations analyzed here are of the photosphere. In order to get a fuller picture of reconnection events, chromospheric and coronal observations must also be considered. Furthermore, solar flares can change the opacity of the solar atmosphere, impacting the accuracy of the photospheric observations and potentially contaminating the data for times during and immediately following a flare.

While the HMI is the first instrument to continuously measure full-disk observations of the solar magnetic field in all orientations (Stanford University, 2019)—an immeasurable value to the advancement of scientific understanding of the Sun—the SHARP catalog is limited to a 12-minute cadence between observations (JSOC, 2019c, 2020). This is because the magnetograms are created using multiple sequences of registered filtergrams, combined using circularly polarized exposures (JSOC, 2020). There are multiple limitations as a result:

- Motions and changes in the magnetic field that occur on time scales less than 12 minutes will be lost

- Observations may be partly or fully affected by the occurrence of a flare during the time between measurements

- For flares that occur between measurements, the times were attributed to the nearest observation time

    - Flare times may be incorrect by as many as six minutes

    - The nearest observation time may be after the start time of the flare, thus resulting in the aforementioned contamination of the data due to the ongoing flare.

IV. Analysis and Results

4.1 Analysis of All Flares

Results for all flares considered in the study can be found in Figure 12. The plots are all in the same time scale, beginning two hours before each flare and concluding four hours after. Arbitrarily, this time window is set as 10:00 to 16:00. The flare time, denoted on the x-axis as 12:00, is represented by the vertical dashed line. The plot of median values of all flares considered is the thick, dashed line. Each of the colored lines represents the median values of the subsets of data that are separated by flare class: blue for B-Class flares, orange for C-Class flares, green for M-Class flares, and red for X-Class flares.

Given that the variability of the X-Class flares prohibits the ability to see trends in smaller flares that are concentrated around the overall median values, the same plots can be see in Figure 13 without the X-Class flares. The scale of the y-axis is set to adjust based on the data displayed, so it shows a much smaller range without the large flares.

Another means of visualizing the data is given in Figure 14. This scatter plot gives the differences from start to end of the epoch time on the y-axis and flare strength along the x-axis. Each of the colors corresponds to flare class, as in Figure 12. Similarly, Figure 15 shows the differences in parameters from start to end time of the flare on the y-axis. This method shows the variability across flare strengths that is lacking in Figures 12 and 13 as all flares studied are shown. Correspondingly, Figures 16 and 17 compare the flare duration to the parameter differences and flare strength, respectively. Parameter values are normalized to flare start time.

The area of active pixels, or size of the active region, increases steadily through-out the six-hour window for B-, C-, and M-Class flares. The ARs of X-Class flares,

however, decrease in size throughout the time. There is a slight leveling trend following the flare for about two hours for these strong flares. A similar trend could be assessed in M-Class flares for a smaller period of time.

Similarly, the total unsigned flux increases more significantly for B- and C-Class flares than it does for M- and X-Class flares. While the B- and C-Class flares range from a half percent lower to a full percent higher from the beginning to end of the epoch analysis, the M-Class flare unsigned flux remains fairly steady and the X-Class unsigned flux has large oscillations around the normalized flare value with an increase beginning 2-3 hours after the flare.

The mean inclination angle, or deviation of the magnetic field lines from radial, decreases slightly among B- and M-Class flares with the strongest signature seen in the B-Class flares. For the C-Class flares, the inclination angle remains steady throughout the duration of the epoch analysis. For the X-Class flares, there is a small spike then a significant decrease in the inclination angle following the flare.

The mean value of the total, vertical, and horizontal field gradients do not have much of a signature in either the B- or C-Class flares. For all three parameters, these smaller flares decrease slightly, but have an overall change of around half a percent. However, both the M- and X-Class flares have similar trends, but at differing scales. Both classes have a strong increase around the flare time with steady elevated levels for a few hours following the flare before returning to normal.

Trends in the mean vertical current density are unlike any of the other parameter trends. For the B-, C-, and M-Class flares, there is a sharp peak at the start of the flare, though it is best defined for the B- and C-Class flares. Meanwhile, for the X-Class flares, there is a decrease to a minimum during the time of the flare. For both of these respective changes, the extrema are significant compared to the values at the beginning and end of the epoch analysis.

The total unsigned vertical current trends are again small. The B- and C-Class flares show an increased unsigned vertical current leading into the flare followed by steady levels. The larger flares, however, show greater variability about the normalized flare value throughout the time period with an overall decrease about one hour following the flare.

The characteristic twist parameter, helicity parameters, and the sum of the absolute value of the net vertical currents per polarity exhibit similar trends, especially for M- and X-Class flares. For all but the sum of the absolute value of the net vertical currents per polarity, the B- and C-Class flares have a slight increase leading up to the flare followed by a steadier decline. Meanwhile, the M- and X-Class flares have sudden increases immediately following the commencement of the flare. In the characteristic twist parameter, absolute value of the net vertical current helicity, and sum of the absolute value of the net vertical currents per polarity, these increases are particularly large for the M-Class flares (the increases are large for X-Class flares for all these parameters).

Mean photospheric excess magnetic energy density decreases slightly for small flares about three hours following the flare. This signal is strongest in B-Class flares. For M-Class flares, there is a slight increase prior to and immediately following the flare and then a slight decrease about one hour afterwards. For X-Class flares, there is a sudden increase in mean photospheric excess magnetic energy density immediately following the flare, continuing for about three hours before beginning to decrease.

Total photospheric magnetic energy density has a similar decreasing trend among all flare classes beginning 2-3 hours following the flare. However, the B-, C-, and M-Class flares all exhibit a slight increase in total photospheric magnetic energy density leading into the flare and X-Class flares have a sharp decrease an hour prior followed by steady levels nearing the flare time.

Both the mean shear angle and the percentage of pixels with a mean shear angle greater than 45° have similar results, which is to be expected given their relationship with each other. The B-, C-, and M-Class flares have a slight decrease during this time with the C- and M-Class flare percentages of pixels with a mean shear angle greater than 45° leveling off following the flare. For the X-Class flares, there is a significant decrease in both parameters beginning about one time step following the start of the flare.

For all parameters, the X-Class flare trends differ from the smaller flare trends. Furthermore, the M-Class flare trends for some parameters or part of the epoch timeline differ from the smaller flares. In these instances, the overall trends are similar to the X-Class flares but to a smaller extent. A similar result was found in Mason and Hoeksema (2010) in which the percent changes in calculated parameters were greater for X-Class flares while the M-Class flares and lower had similar changes. This indicates that the large flares are outliers among solar flares. Interestingly, the changes from the start to end of the epoch analysis and of the flare duration show greater variation among smaller flares than larger for all parameters (Figures 14, 15, and 16).

The greatest change over the duration of the flare (Figures 15 and 16) manifests in the mean vertical current density, with multiple instances of changes up to 40 times greater or less than the value at the flare start. The majority of the events are within 20 times the start value, which still provides the greatest change in parameter value. The next closest are the characteristic twist parameter, mean vertical current helicity, and absolute value of the net vertical current helicity, whose changes are concentrated within 10 times the initial value.

Figure 17 shows that the majority of flares last for less than 100 minutes. The longest flares seem to be the upper-B-Class and lower-C-Class flares, which is also

where the strength distribution peaks (Figure 2). Moreover, the shortest flares change the most over the duration of the flare (Figure 16). Given that these shortest flares comprise a majority of the dataset, they are likely to best represent flare magnetic field properties.

4.2 Analysis of B-Class Flares

Results for B-Class flares can be found in Figure 18. The axes are set up in the same manner as the plots for all flares. For these plots, the thick, dashed line denotes the median values for the subset of B-Class flares. Each colored line shows the median values for each further subset of flare strengths: red for flares with strengths B1.0-B1.9, orange for flares with strengths B2.0-B2.9, yellow for flares with strengths B3.0-B3.9, green for flares with strengths B4.0-B4.9, blue for flares with strengths B5.0-B5.9, purple for flares with strengths B6.0-B6.9, pink for flares with strengths B7.0-B7.9, brown for flares with strengths B8.0-B8.9, and gray for flares with strengths B9.0-B9.9.

In addition to trends discussed in the previous section, a few patterns can be found when looking at a breakdown of B-Class flare strengths. For both the area of active pixels and total unsigned flux, all B-Class flares increase significantly over the time period. However, some of the larger B-Class flares have smaller changes after the flare occurs. The changes for active pixel area range from -1% before the flare to 1% after the flare, with the greatest changes seen in the B3 and B5 flares. Gradient parameters as well as some of the vertical current parameters and energy density parameters, which have little change for all B-Class flares considered, seem to have an increased variability among sub-classes particularly beginning one hour after the flare begins. Finally, the unique trend in mean vertical current density seen for B-, C-, and M-Class flares is found particularly in the low- to mid-B-Class flares.

33

4.3 Analysis of C-Class Flares

Results for C-Class flares can be found in Figure 19. The axes are set up in the same manner as before. For these plots, the thick, dashed line denotes the median values for the subset of C-Class flares. Each colored line shows the median values for each further subset of flare strengths: red for flares with strengths C1.0-C1.9, orange for flares with strengths C2.0-C2.9, yellow for flares with strengths C3.0-C3.9, green for flares with strengths C4.0-C4.9, blue for flares with strengths C5.0-C5.9, purple for flares with strengths C6.0-C6.9, pink for flares with strengths C7.0-C7.9, brown for flares with strengths C8.0-C8.9, and gray for flares with strengths C9.0-C9.9.

Similar to the B-Class flares, there are a few trends that can be expanded upon from this closer look into sub-class analysis. For the strongest C-Class flares, there are unique decreasing trends in the gradient parameters following a flare. The C8 flare gradients increase leading into and immediately following the flare (similar to the M- and X-Class flares, previously discussed) but begin to decline about one hour following. Meanwhile, the C9 flare gradients decrease into and immediately following the flare before leveling out in the period 1-2 hours after the flare. Again, the C8 flares differ in the mean vertical current density in which the trend actually resembles closer to that of the X-Class flares than the particular trend of the B-, C-, and M-Class flares. The remainder of the parameters have fairly neutral overall changes during the time period considered for all C-Class flares with variabilities among the sub-classes, particularly the mid- and high-C-Class flares.

4.4 Analysis of M-Class Flares

Results for M-Class flares can be found in Figure 20. The axes are set up in the same manner as before. For these plots, the thick, dashed line denotes the median values for the subset of M-Class flares. Each colored line shows the median values for

each further subset of flare strengths: red for flares with strengths M1.0-M1.9, orange for flares with strengths M2.0-M2.9, yellow for flares with strengths M3.0-M3.9, green for flares with strengths M4.0-M4.9, blue for flares with strengths M5.0-M5.9, purple for flares with strengths M6.0-M6.9, pink for flares with strengths M7.0-M7.9, brown for flares with strengths M8.0-M8.9, and gray for flares with strengths M9.0-M9.9.

Again, closer inspection into sub-M-Class flares reveals a few trends that are unseen in the overall analysis. Unlike the smaller flares, there is significant variation in the AR size and amount of unsigned flux, particularly in M4 flares and larger. Area variations range from -2% to 4% from the flare time values and the trends themselves do not follow the same increasing tendency throughout the entire window. For the unsigned flux, most of these larger M-Class flares actually decrease leading into the flare. In the gradient parameters, the M8 flares increase into and following the flare, just as the X-Class flares do. For the mean vertical current density, the previously discussed peak at flare time is harder to see due to the variation among high-M-Class flares throughout the entire window. Looking closely at the flare time, the smaller M-Class flares seem to follow closer to the overall M-Class median values. Notably, however, the larger M-Class flares do not seem to follow the same trends seen in the X-Class flares, nor is there much of a conceivable trend at all.

For the remainder of the parameters, particularly the helicity and twist parameters, there is great variation among the M9 flares relative to the overall M-Class medians. A possible explanation for this volatility in the stronger flares could be the small sample size (see Table 2). This poses difficulty in deducing trends for these larger flare sub-classes as well as the entirety of the X-Class flare subset.

4.5 Analysis of X-Class Flares

Results for X-Class flares can be found in Figure 21. The axes are set up in the same manner as before. For these plots, the thick, dashed line denotes the median values for the subset of X-Class flares. Each colored line shows the median values for each further subset of flare strengths: red for flares with strengths X1.0-X1.9, orange for flares with strengths X2.0-X2.9, yellow for flares with strengths X3.0-X3.9, green for flares with strengths X4.0-X4.9, blue for flares with strengths X5.0-X5.9, purple for flares with strengths X6.0-X6.9, pink for flares with strengths X7.0-X7.9, brown for flares with strengths X8.0-X8.9, and gray for flares with strengths X9.0-X9.9. As discussed in the Methodology section, flares of strength X4 and greater are discarded as outliers using the applied masks.

Once more, trends deduced from sub-class analysis may give greater insight into the trends already discussed for the analysis of all flares. As with the M-Class flares, the small sample size of strong flares leads to difficulty in assessing trends. Related, the X-Class medians are dominated significantly by the X1 flares, which make up 73% of this class. The twist and helicity parameters again prove to be of significant note in this subset. Particularly, the sudden increase in these parameter values following the flare increases in slope for increasing flare strength, to as much as two times the flare value.

4.6 Results

Similar to the small flare case study (see Methodology), the B-, C-, and M-Class flares increase in size and unsigned flux throughout the entire epoch analysis, indicating that the ARs are growing while the X-Class flare ARs might have reached a maximum in size and strength. Additional trends suggest that there are differences in the underlying physics associated with small and large flares. The behavior of the

X-Class and, to a lesser extent, the M-Class flares differs from that of the B- and C-Class flares. Within the sub-classes of M-Class flares, there appears to be a change from behaviors of smaller flares to those of larger flares.

Notably, the twist and helicity parameters have a significant increase after the onset of a strong flare. This indicates greater twisting of the magnetic field lines following the flare, perhaps a reaction to untwisting during the flare. There is also an intensifying throughout these flare processes, seen by the increase in gradient parameters.

Consistent with Bobra and Couvidat (2015), parameters focusing on total unsigned vertical current are among those with the strongest visible trends. From this study, the helicity parameters as well as the twist parameter, in particular, exhibit similar trends. Of note, however, Bobra and Couvidat (2015) find these parameters to be beneficial for flare forecasting, while this study indicates that the trends are better seen following the flare.

For the purposes of flare forecasting, few of the parameters give an overwhelming signature associated with an imminent flare, with the exception of the mean vertical current density. The strong increase leading into the flare start may give an early indication of an AR that is soon to flare, increasing as much as a full percent within the hour prior to the flare. For the M-Class flares, there are other spikes in the data for this parameter that may provide false-positive forecasts. However, this parameter may be of significant use for forecasting of B- and C-Class flares.
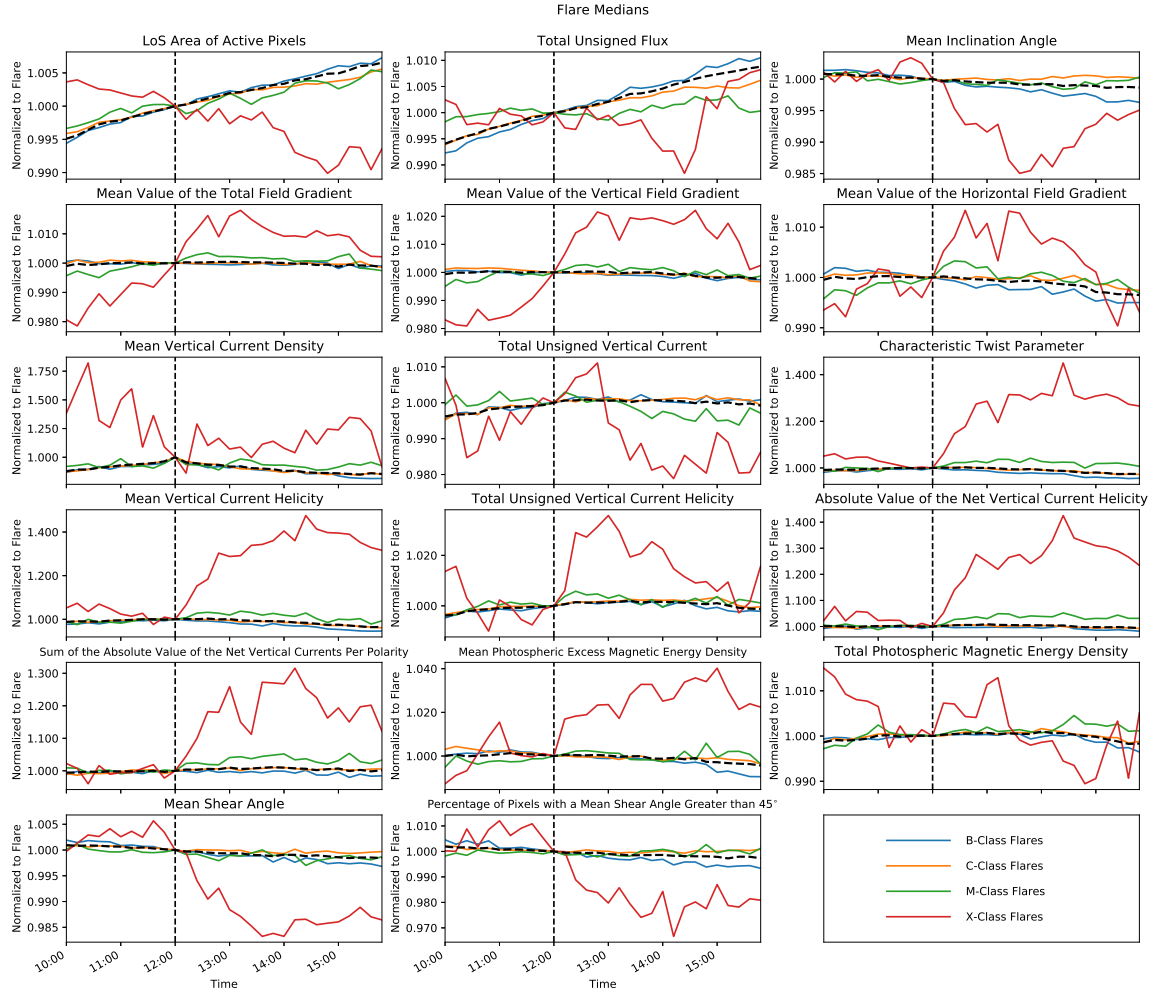
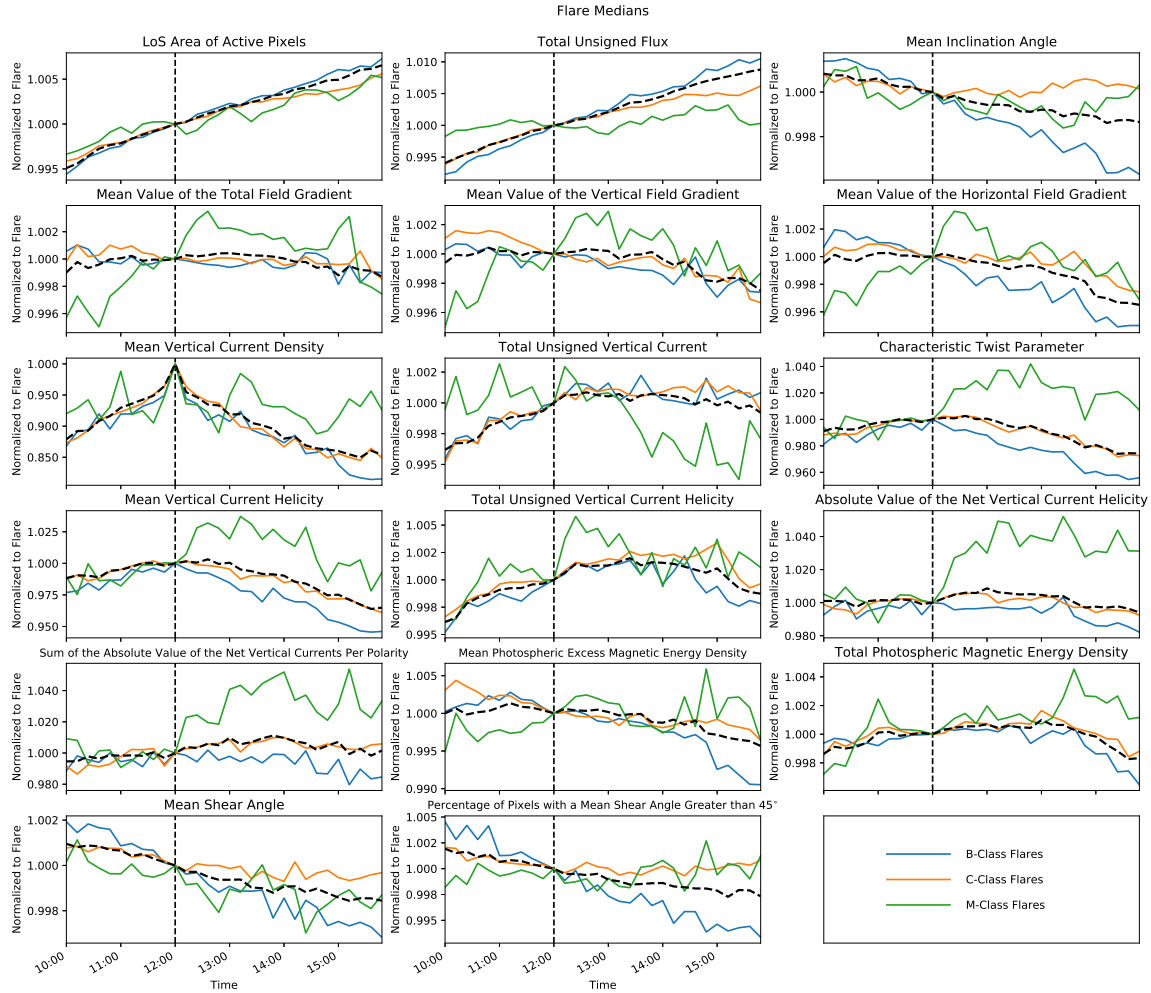**Figure 12.** Epoch analysis for all flares between May 2010 and September 2019. All data are normalized to the values at the time of the flare, which is identified as the dashed vertical line. Strengths of flares are separated by corresponding colors. The plots display medians for all events in the associated flare class. Flares outside of three standard deviations from the average and outside of 70° heliographic longitude are excluded as outliers. SHARP data are acquired from JSOC using the Python notebook created by Glogowski and Bobra (2016) and flare times are identified by SWPC (2019).

38

Figure 13. Epoch analysis for all but X-Class flares between May 2010 and September 2019. All data are normalized to the values at the time of the flare, which is identified as the dashed vertical line. Strengths of flares are separated by corresponding colors. The plots display medians for all events in the associated flare class. Flares outside of three standard deviations from the average and outside of 70° heliographic longitude are excluded as outliers. SHARP data are acquired from JSOC using the Python notebook created by Glogowski and Bobra (2016) and flare times are identified by SWPC (2019).
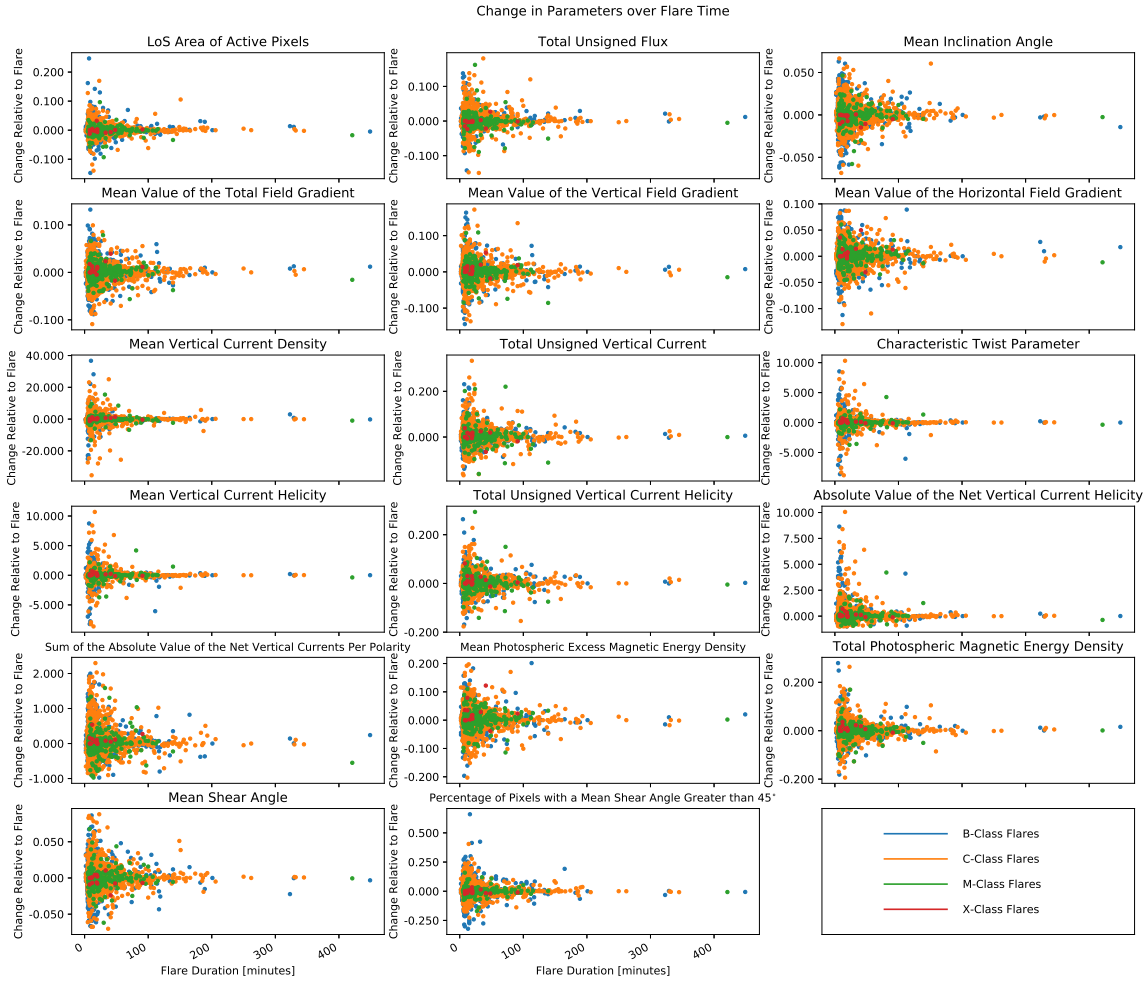
39
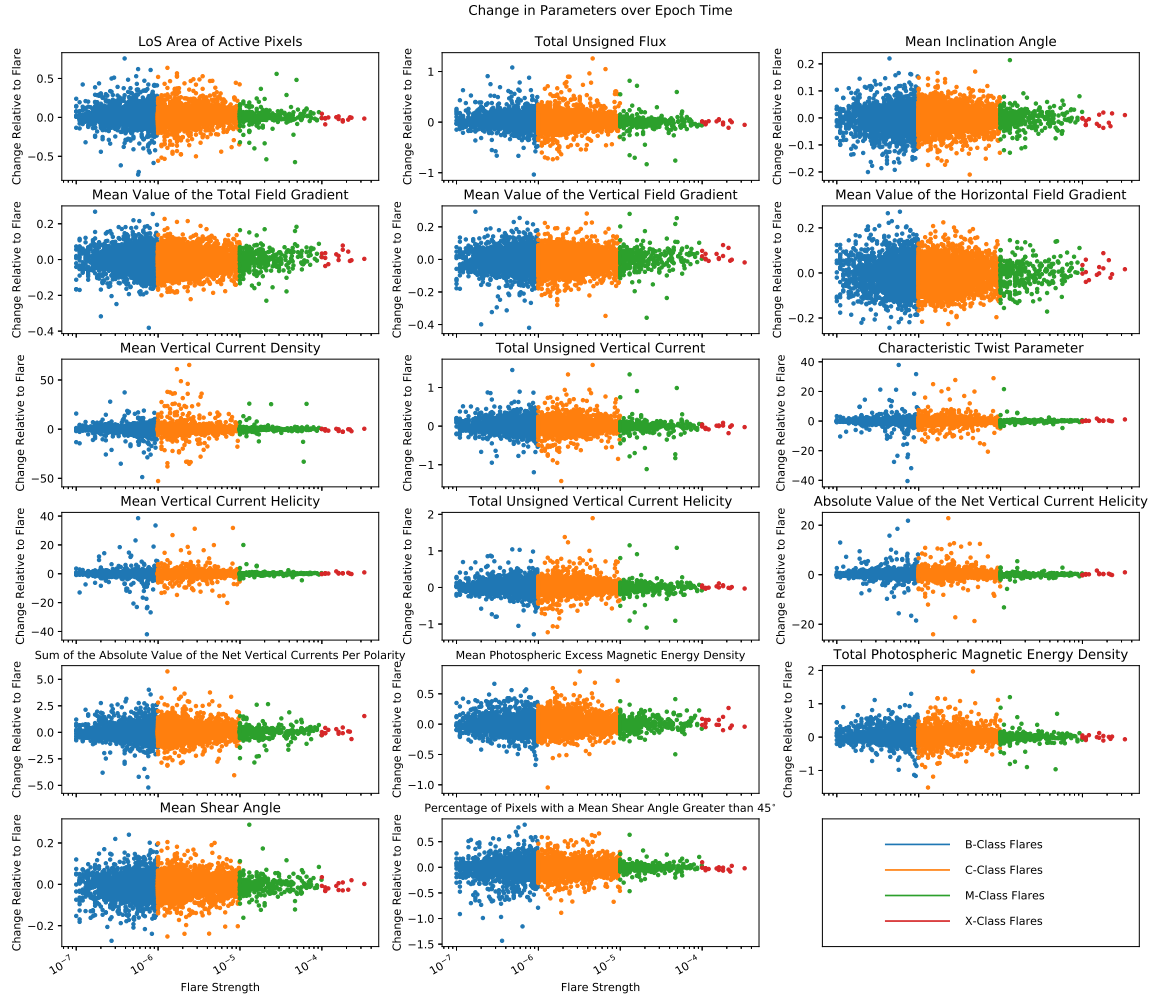
Figure 14. **Differences in normalized parameter values from two hours prior to four hours after the start time of a flare. Strengths of flares are along the semilogarithmic x-axis and separated by flare class with corresponding colors. Flares outside of three standard deviations from the average and outside of 70° heliographic longitude are excluded as outliers. SHARP data are acquired from JSOC using the Python notebook created by Glogowski and Bobra (2016) and flare times are identified by SWPC (2019).**
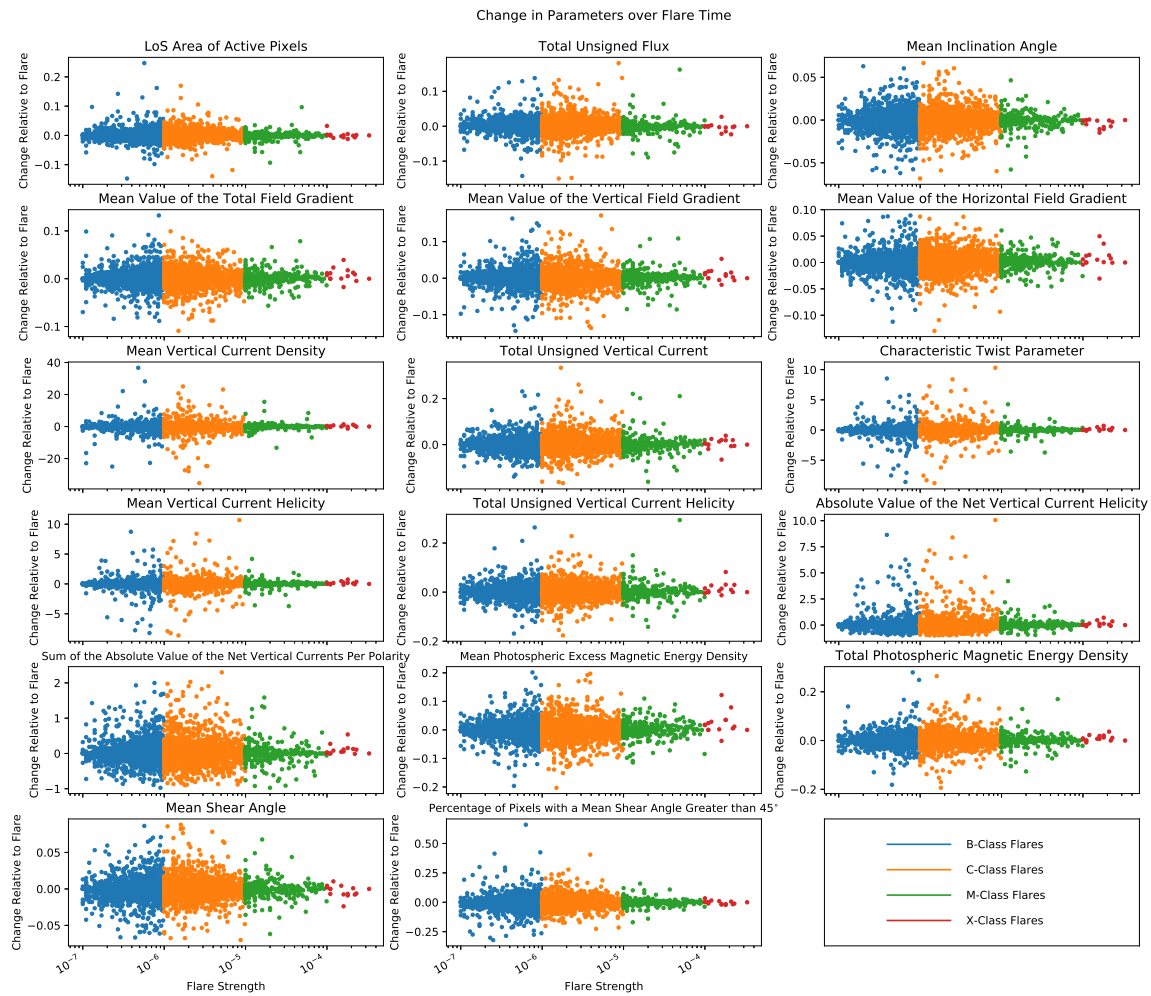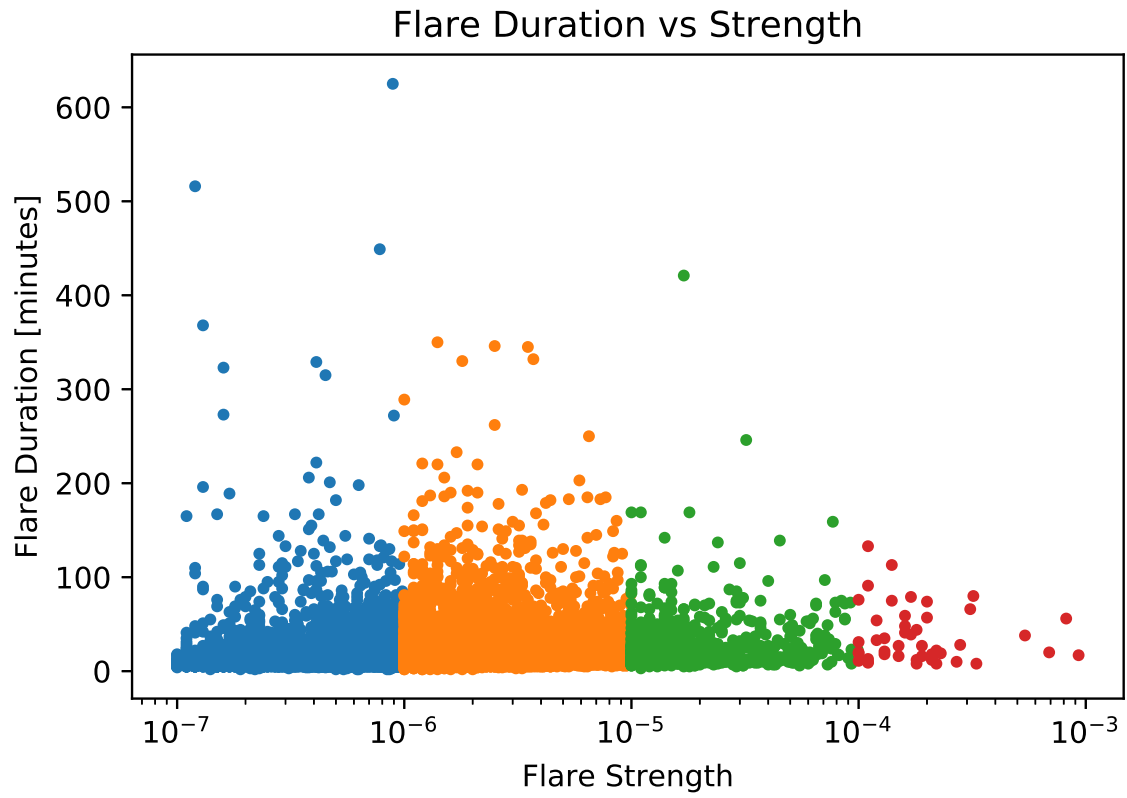
Figure 15. Differences in normalized parameter values from the start to end time of a flare. Strengths of flares are along the semilogarithmic x-axis and separated by flare class with corresponding colors. Flares outside of three standard deviations from the average and outside of $70°$ heliographic longitude are excluded as outliers. SHARP data are acquired from JSOC using the Python notebook created by Glogowski and Bobra (2016) and flare times are identified by SWPC (2019).

Figure 16. Differences in normalized parameter values from start to end time of a flare compared to the duration of the flare. Durations of flares are along the x-axis in minutes and separated by flare class with corresponding colors. Flares outside of three standard deviations from the average and outside of $70°$ heliographic longitude are excluded as outliers. SHARP data are acquired from JSOC using the Python notebook created by Glogowski and Bobra (2016) and flare times are identified by SWPC (2019).

Figure 17. Duration of flares compared to their strengths. Strengths of flares are along the semilogarithmic x-axis and separated by flare class with corresponding colors. Flares outside of three standard deviations from the average and outside of $70°$ heliographic longitude are excluded as outliers. SHARP data are acquired from JSOC using the Python notebook created by Glogowski and Bobra (2016) and flare times are identified by SWPC (2019).
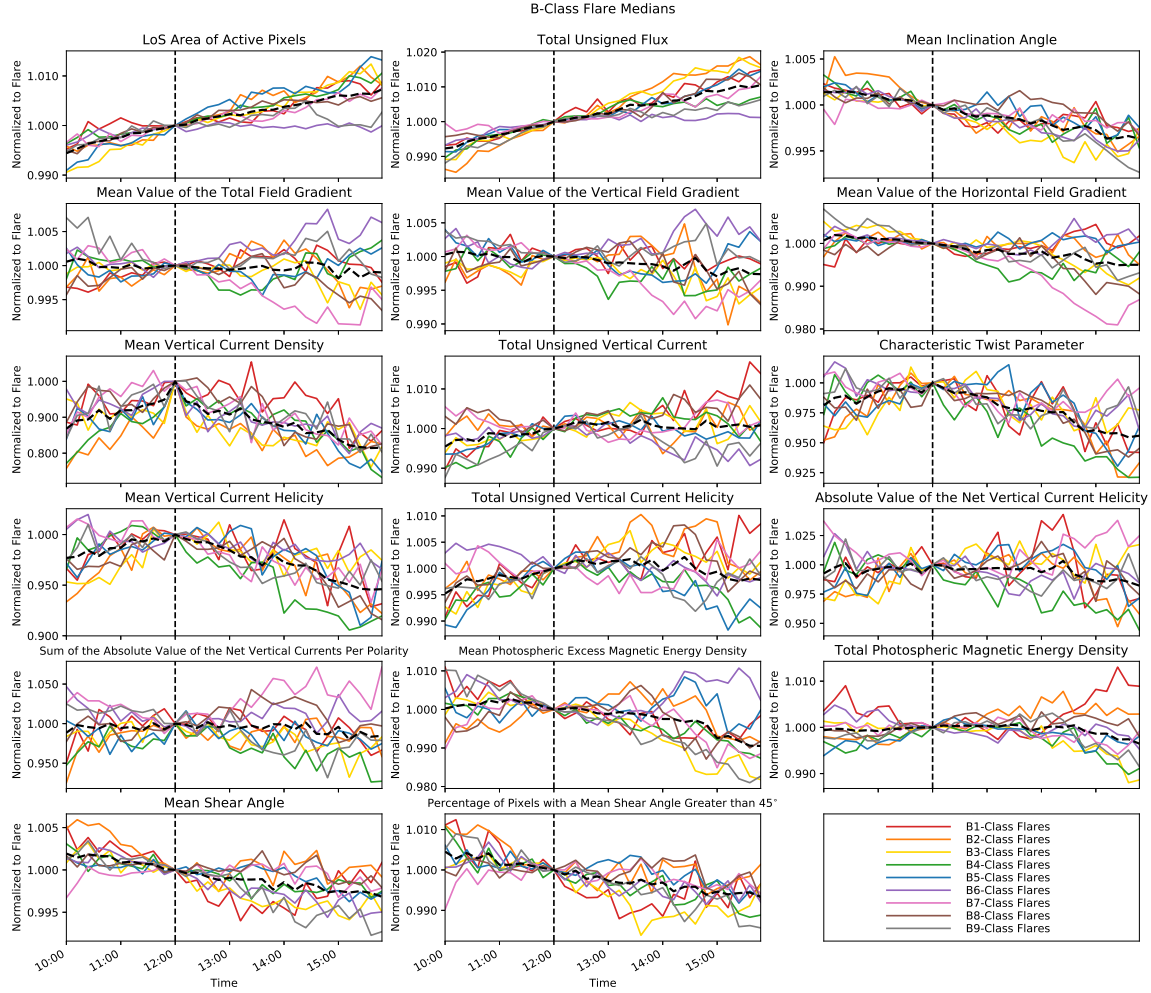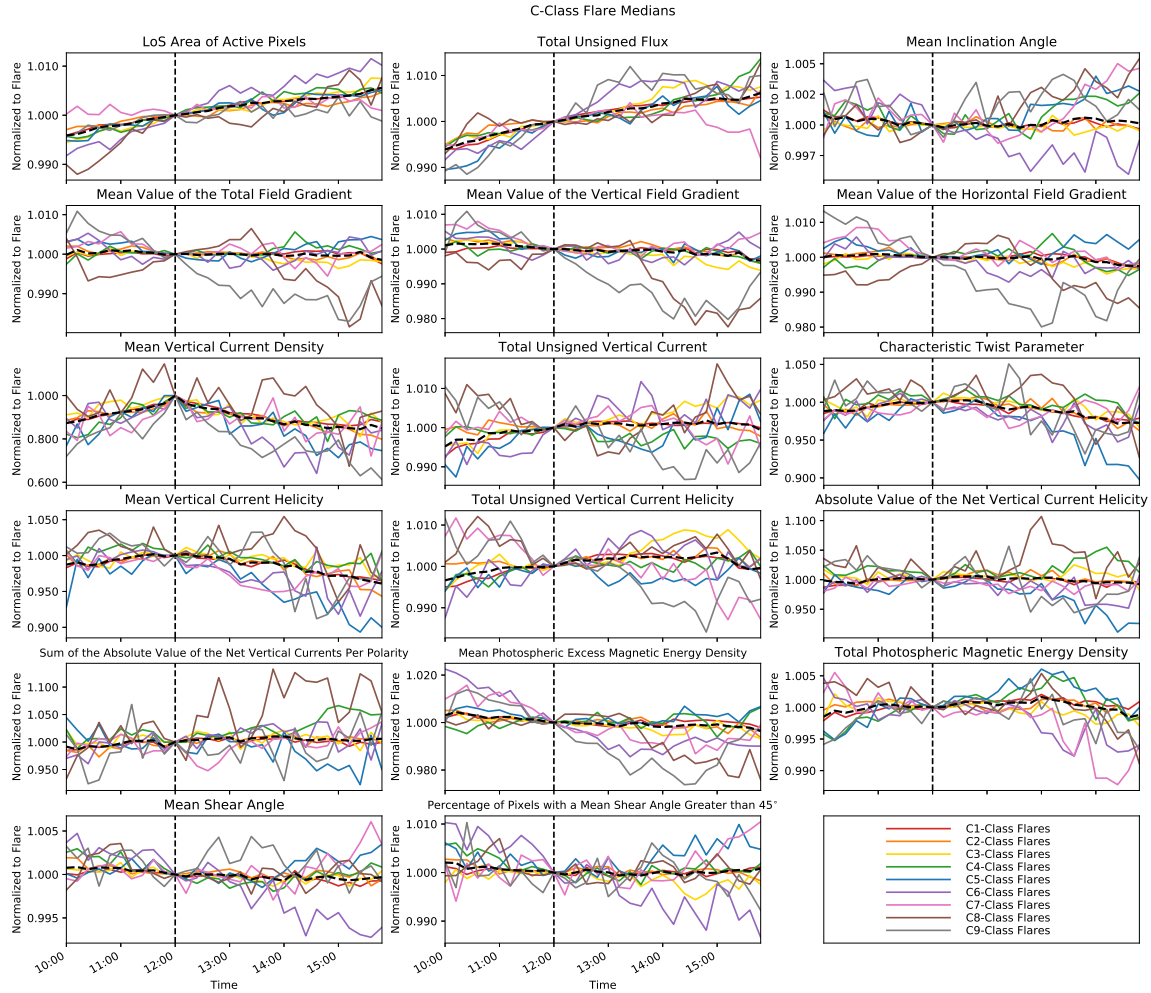
Figure 18. Epoch analysis for B-Class flares between May 2010 and September 2019. All data are normalized to the values at the time of the flare, which is identified as the dashed vertical line. Strengths of flares are separated by corresponding colors. The plots display medians for all events in the associated flare class. Flares outside of three standard deviations from the average and outside of $70°$ heliographic longitude are excluded as outliers. SHARP data are acquired from JSOC using the Python notebook created by Glogowski and Bobra (2016) and flare times are identified by SWPC (2019).
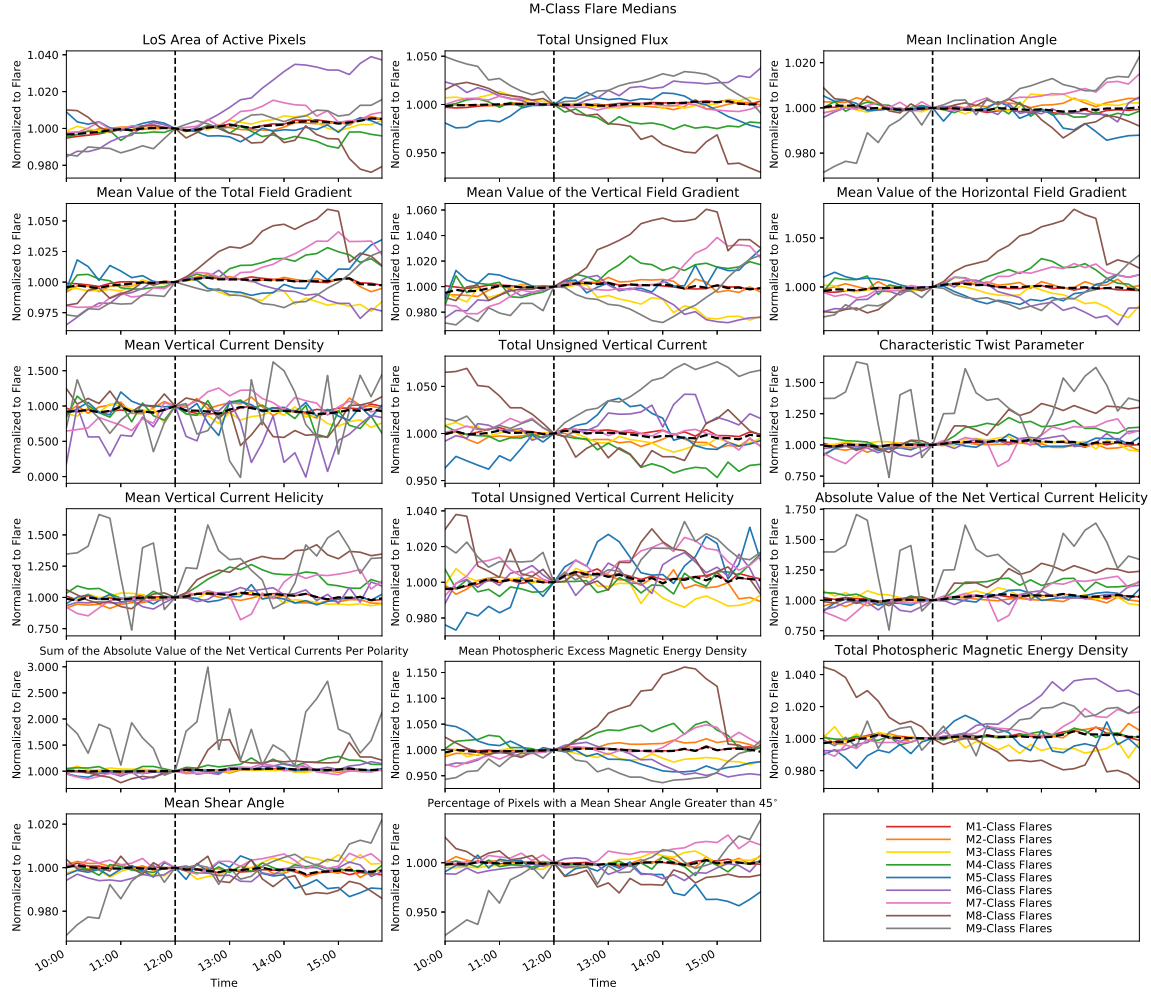
Figure 19. Epoch analysis for C-Class flares between May 2010 and September 2019. All data are normalized to the values at the time of the flare, which is identified as the dashed vertical line. Strengths of flares are separated by corresponding colors. The plots display medians for all events in the associated flare class. Flares outside of three standard deviations from the average and outside of $70°$ heliographic longitude are excluded as outliers. SHARP data are acquired from JSOC using the Python notebook created by Glogowski and Bobra (2016) and flare times are identified by SWPC (2019).
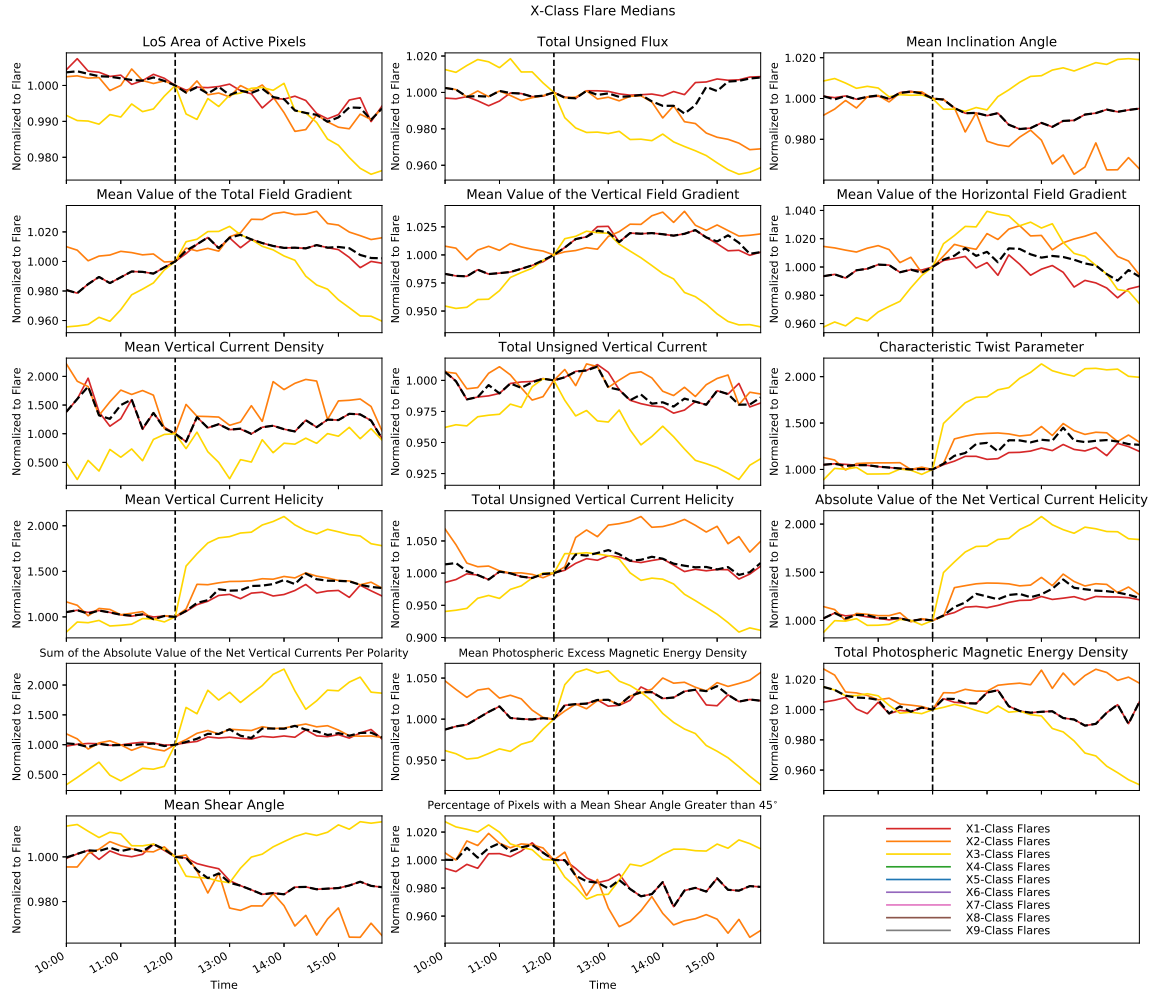
45

Figure 20. Epoch analysis for M-Class flares between May 2010 and September 2019. All data are normalized to the values at the time of the flare, which is identified as the dashed vertical line. Strengths of flares are separated by corresponding colors. The plots display medians for all events in the associated flare class. Flares outside of three standard deviations from the average and outside of $70°$ heliographic longitude are excluded as outliers. SHARP data are acquired from JSOC using the Python notebook created by Glogowski and Bobra (2016) and flare times are identified by SWPC (2019).

Figure 21. Epoch analysis for X-Class flares between May 2010 and September 2019. All data are normalized to the values at the time of the flare, which is identified as the dashed vertical line. Strengths of flares are separated by corresponding colors. The plots display medians for all events in the associated flare class. Flares outside of three standard deviations from the average and outside of $70°$ heliographic longitude are excluded as outliers. SHARP data are acquired from JSOC using the Python notebook created by Glogowski and Bobra (2016) and flare times are identified by SWPC (2019).

V. Conclusions

5.1 Summary

For the purposes of understanding the underlying physics, certain trends can be identified. The rise in both size and flux levels of small and moderate flares indicates that these ARs may still be growing in size and strength while producing flares. The X-Class flares, however, seem to be doing the opposite, perhaps suggesting that they have reached a maximum size or strength. Trends in the field gradients for M- and X-Class flares demonstrate the intensifying of the magnetic structures during the flare process. Similarly, the sudden increase in helicity parameters and characteristic twist parameter following M- and X-Class flares implies an increase in the complexity of the magnetic field configuration. Extreme responses of X-Class flare ARs suggests that they get obliterated by the flares.

Coupled with the changes noted in Figures 14 and 15, in which helicity and twist parameters show greatest variability throughout the flare duration, these parameters provide a strong signal for investigation into the physics of flares. Of note, these all rely on the vertical current density, but the mean vertical current density and total unsigned vertical current parameters do not exhibit similar patterns in the epoch analysis (Figures 12 and 13). The mean vertical current density does show the greatest variability in the change over the course of the flare (Figures 15 and 16).

As previously stated, Figure 12 suggests that X-Class flares are outliers among the dataset. Furthermore, the shorter events, particularly of the B-, C-, and M-Class flares, exhibit the greatest variability and makeup the majority of the dataset (Figures 16 and 17). Given that the B-Class flares are harder to sample and often left out of databases (Figure 2) and that M-Class flares follow similar trends to the X-Class flares, both with small sample sizes (Figure 13), the C-Class flares prove to be a

48

significant subset of the overall dataset. Moving forward, studies focused specifically on C-Class flares may be more indicative of basic flare physics.

For the purposes of forecasting flares, however, few of these parameters show strong patterns. The most significant trend leading into a flare seems to be the mean vertical current density, particularly for B-, C-, and M-Class flares. This could be helpful as these flares are often harder to predict. Anecdotally, large flares can be expected from extremely complex ARs with only a question of timing whereas smaller and less complex ARs have a higher chance of not producing a flare. However, the signature manifests within the hour leading into the flare, which does not give much of a lead time for the flare forecast.

5.2 Future Work

5.2.1 Flare Classification

The current flare classification separates events based solely on their maximum x-ray flux. Apart from general trends, this classification does not adequately separate flares by common behavior. Furthermore, due to the high volume of flares in the HMI dataset, it is difficult to determine overall trends. Separating the flares based on commonalities between the events or ARs would serve to better classify flare types and trends and could benefit flare forecasting. For example, a flare classification based on AR properties could be used by forecasters to identify possible events produced from similar observations in real time. Some of the ways that the flare database could be further broken down in order to assess trends include:

- Comparing flares that occur as the AR is near solar meridian to those that occur when the AR is near solar limbs

- Correlating flares with geo-effective events such as coronal mass ejections (CMEs)

and compare to flares without these events

- Determining whether the occurrence of a precursor flare, as in Verma (2018), impacts the resulting parameters

- Studying the differences in flare properties throughout the evolution of the AR lifetime.

5.2.2 Statistical Analysis

The statistical analysis performed in this study is limited to basic statistics, namely means, medians, and standard deviations. However, further research into the distribution of the parameters for a given time across flare strengths—and appropriate analysis—could better provide a characterization of the parameters in question.

Another improvement to statistical analysis of these flares could be to further mask the imagery to isolate the parts of the AR that most impact the magnetic reconnection. One option would be to use the flare ribbon database created by Kazachenko et al. (2017) to then calculate magnetic parameters for the footprints of the reconnection flux tubes. A similar option would be to identify the polarity inversion line and calculate the parameters for pixels identified along that line in order to eliminate pixels in the AR that contain weak magnetic fields, as in Bobra and Couvidat (2015) and Mason and Hoeksema (2010).

In a similar matter, improving the spatial scope of the events considered would include more events. To be able to accurately use data with greater deviations from disk center, a deconvolution algorithm to compensate for limb darkening effects such as that in Criscuoli et al. (2017) could be applied. Improving flare statistics and categorizations can provide greater trend analysis for both improved physics understanding and forecasting abilities of solar flares of all strengths.
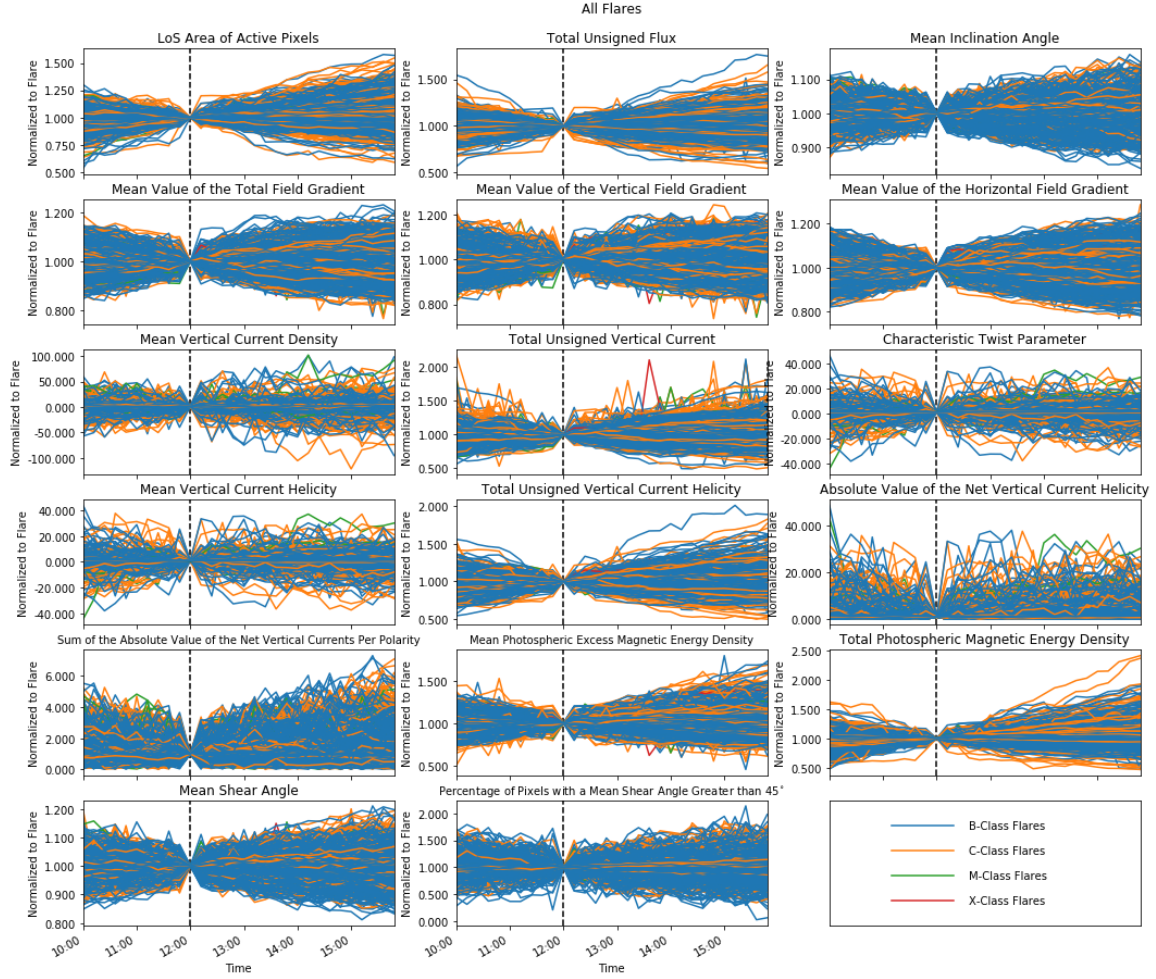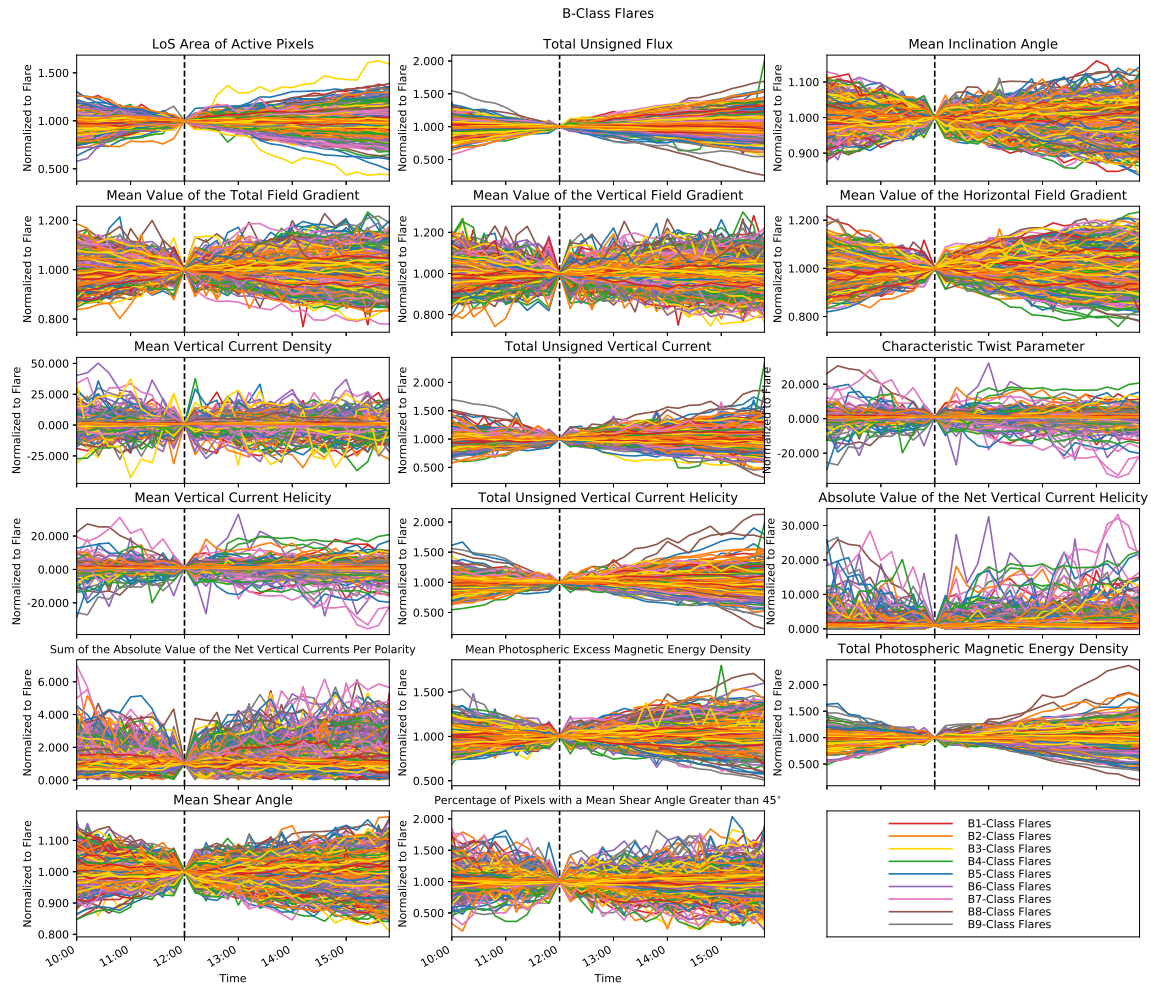
Flares Included in Analysis

Figure 22. Epoch analysis for all flares between May 2010 and September 2019. All data are normalized to the values at the time of the flare, which is identified as the dashed vertical line. Strengths of flares are separated by corresponding colors. Flares outside of three standard deviations from the average and outside of $70°$ heliographic longitude are excluded as outliers. SHARP data are acquired from JSOC using the Python notebook created by Glogowski and Bobra (2016) and flare times are identified by SWPC (2019).
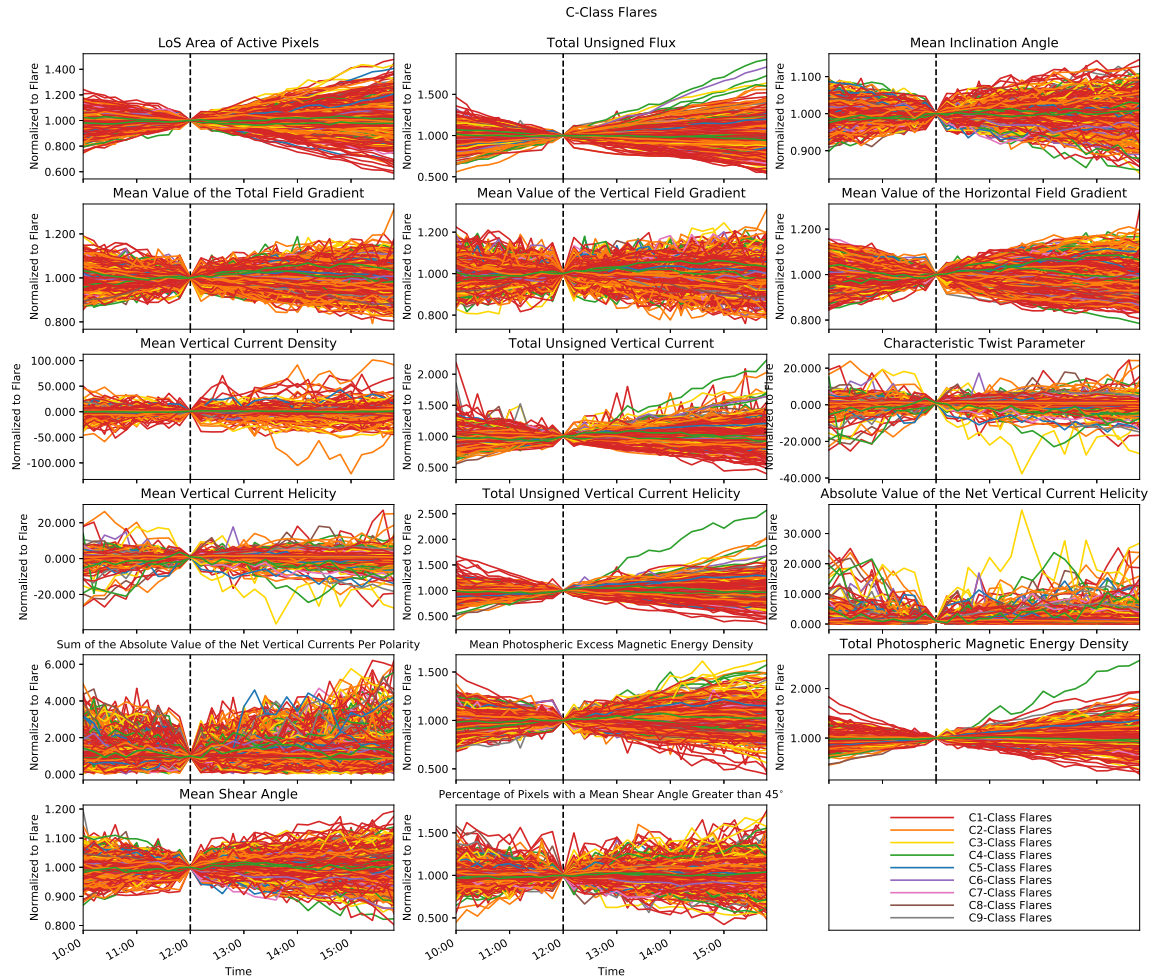
Figure 23. Epoch analysis for B-Class flares between May 2010 and September 2019. All data are normalized to the values at the time of the flare, which is identified as the dashed vertical line. Strengths of flares are separated by corresponding colors. Flares outside of three standard deviations from the average and outside of $70°$ heliographic longitude are excluded as outliers. SHARP data are acquired from JSOC using the Python notebook created by Glogowski and Bobra (2016) and flare times are identified by SWPC (2019).
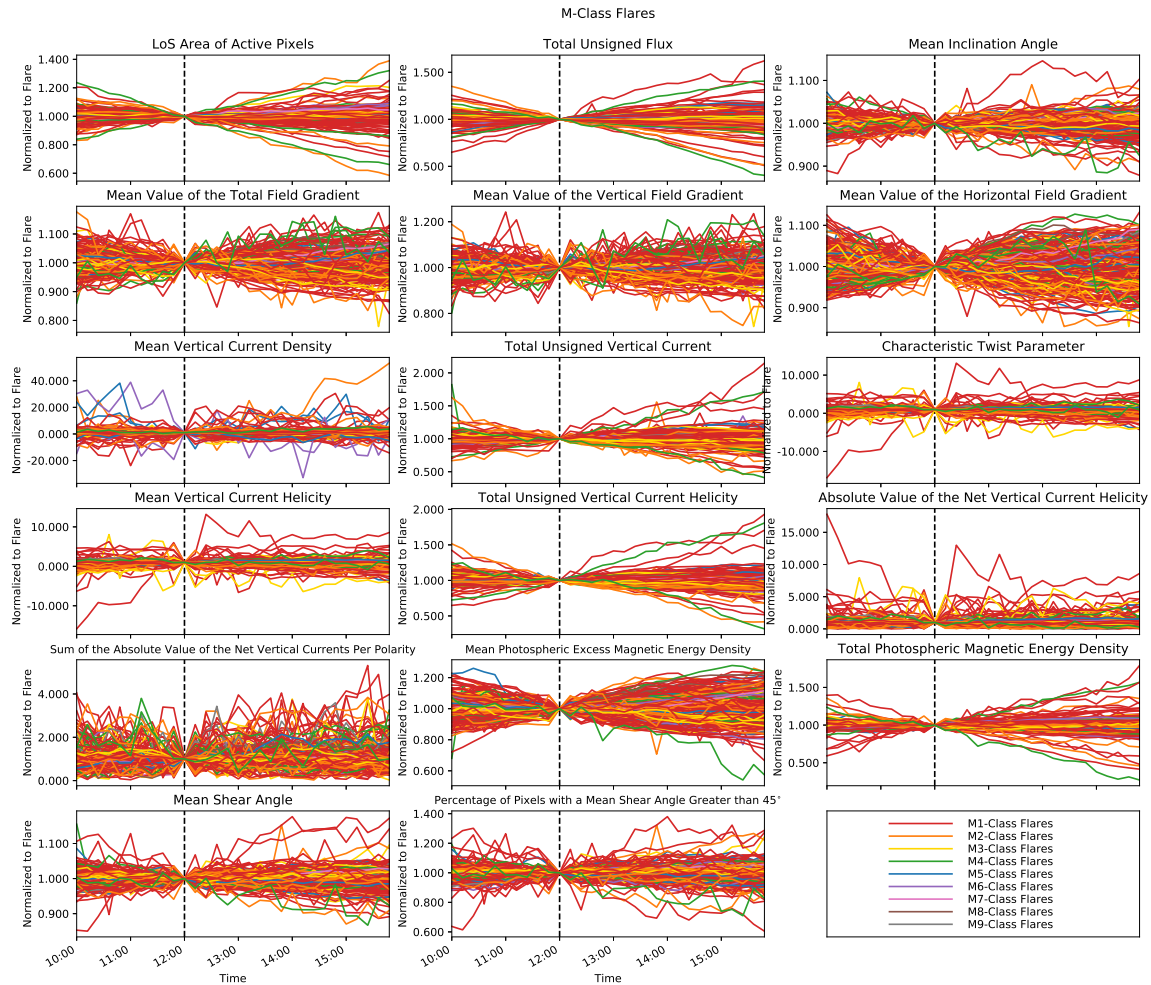
Figure 24. **Epoch analysis for C-Class flares between May 2010 and September 2019. All data are normalized to the values at the time of the flare, which is identified as the dashed vertical line. Strengths of flares are separated by corresponding colors. Flares outside of three standard deviations from the average and outside of $70°$ heliographic longitude are excluded as outliers. SHARP data are acquired from JSOC using the Python notebook created by Glogowski and Bobra (2016) and flare times are identified by SWPC (2019).**
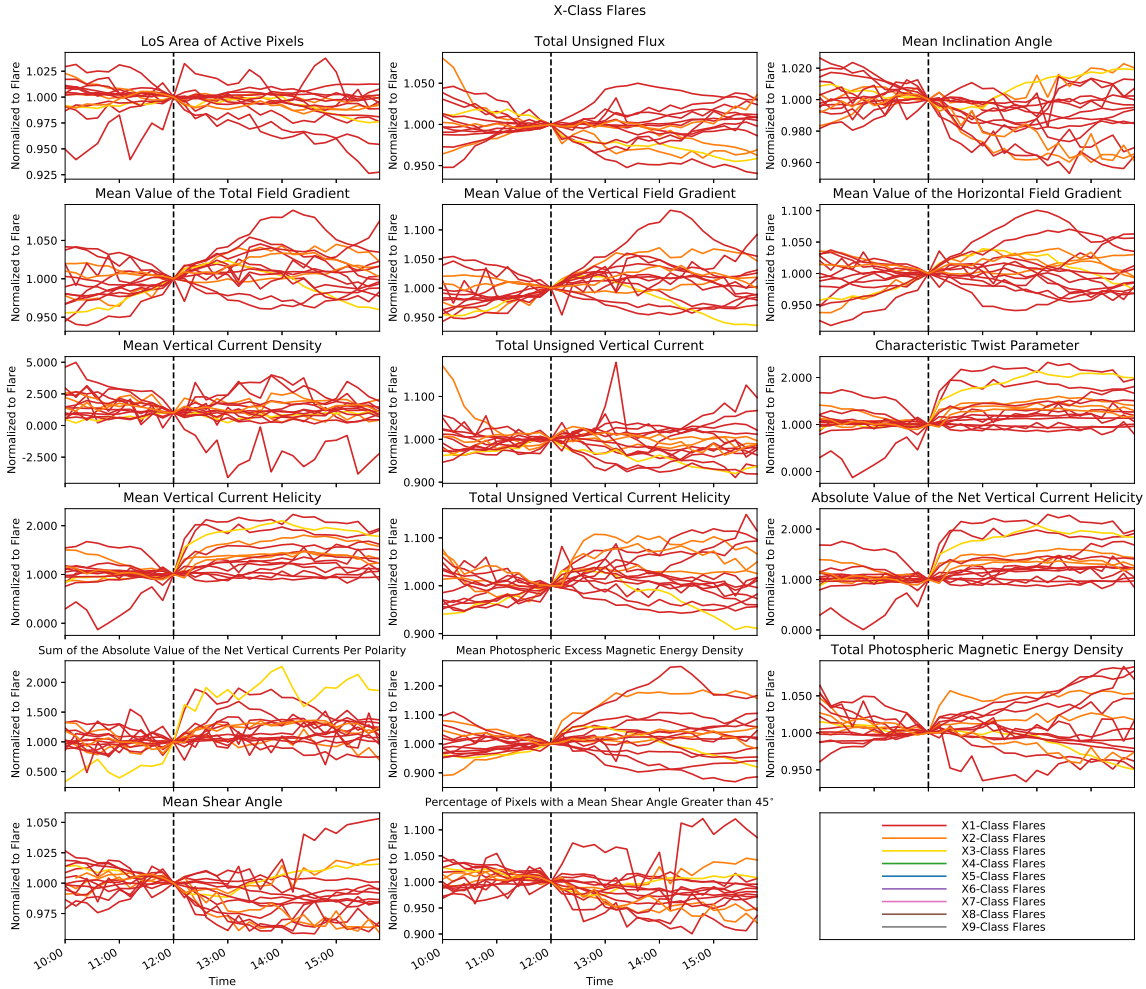
Figure 25. Epoch analysis for M-Class flares between May 2010 and September 2019. All data are normalized to the values at the time of the flare, which is identified as the dashed vertical line. Strengths of flares are separated by corresponding colors. Flares outside of three standard deviations from the average and outside of $70°$ heliographic longitude are excluded as outliers. SHARP data are acquired from JSOC using the Python notebook created by Glogowski and Bobra (2016) and flare times are identified by SWPC (2019).

Figure 26. Epoch analysis for X-Class flares between May 2010 and September 2019. All data are normalized to the values at the time of the flare, which is identified as the dashed vertical line. Strengths of flares are separated by corresponding colors. Flares outside of three standard deviations from the average and outside of $70°$ heliographic longitude are excluded as outliers. SHARP data are acquired from JSOC using the Python notebook created by Glogowski and Bobra (2016) and flare times are identified by SWPC (2019).
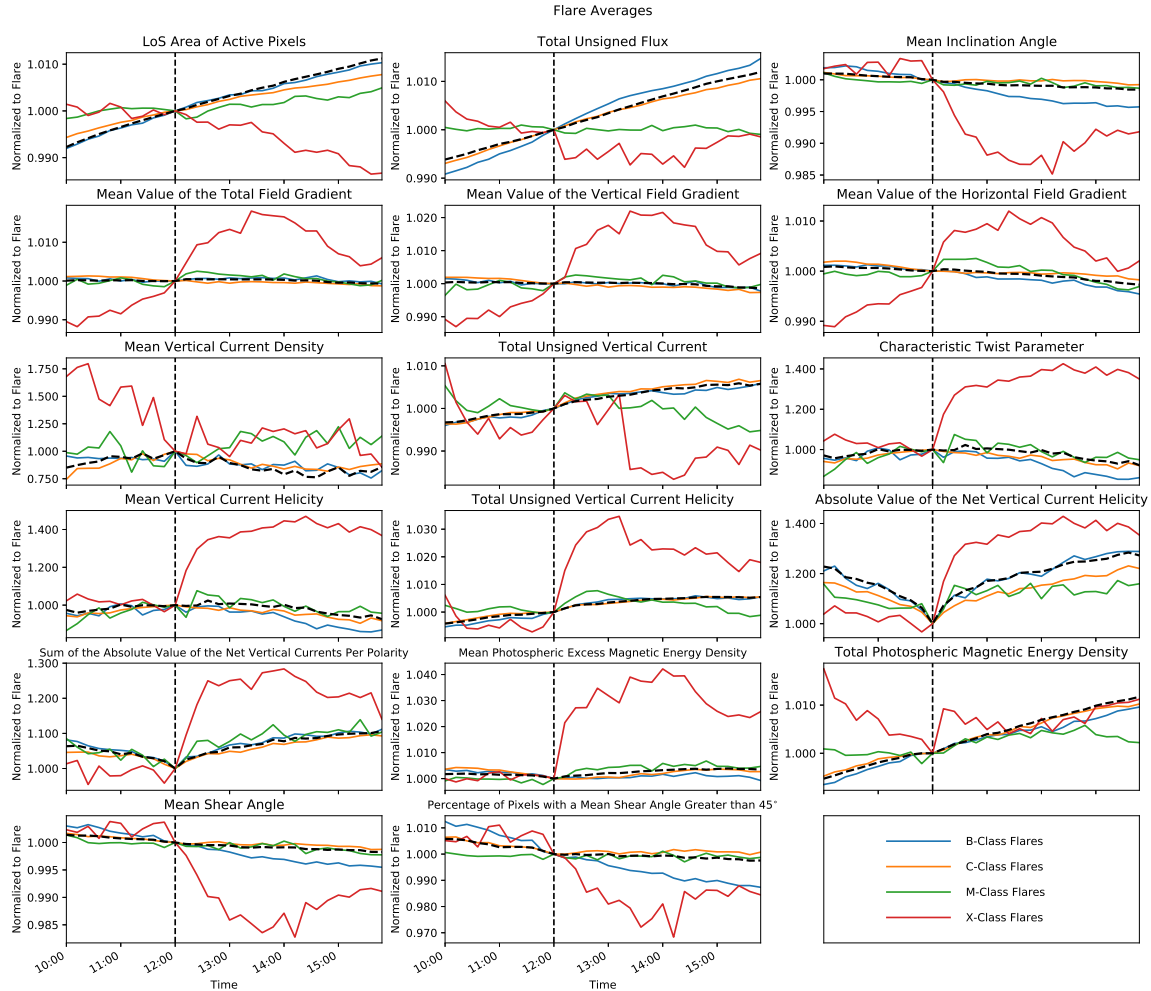
Appendix B

Flare Average Plots

Figure 27. Epoch analysis for all flares between May 2010 and September 2019. All data are normalized to the values at the time of the flare, which is identified as the dashed vertical line. Strengths of flares are separated by corresponding colors. The data are averaged for all events in the associated flare class. Flares outside of three standard deviations from the average and outside of $70°$ heliographic longitude are excluded as outliers. SHARP data are acquired from JSOC using the Python notebook created by Glogowski and Bobra (2016) and flare times are identified by SWPC (2019).
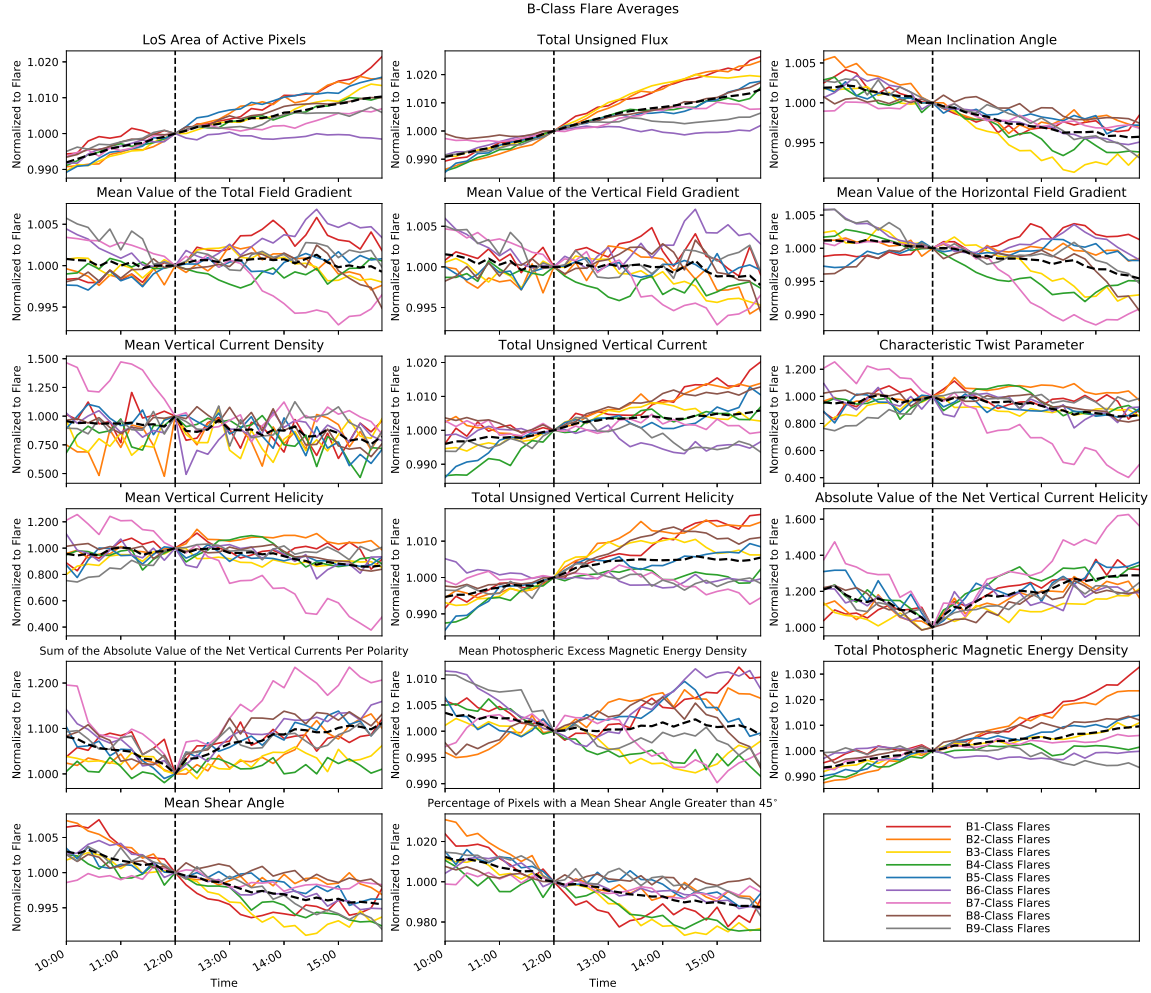
Figure 28. **Epoch analysis for B-Class flares between May 2010 and September 2019. All data are normalized to the values at the time of the flare, which is identified as the dashed vertical line. Strengths of flares are separated by corresponding colors. The data are averaged for all events in the associated flare class. Flares outside of three standard deviations from the average and outside of $70°$ heliographic longitude are excluded as outliers. SHARP data are acquired from JSOC using the Python notebook created by Glogowski and Bobra (2016) and flare times are identified by SWPC (2019).**
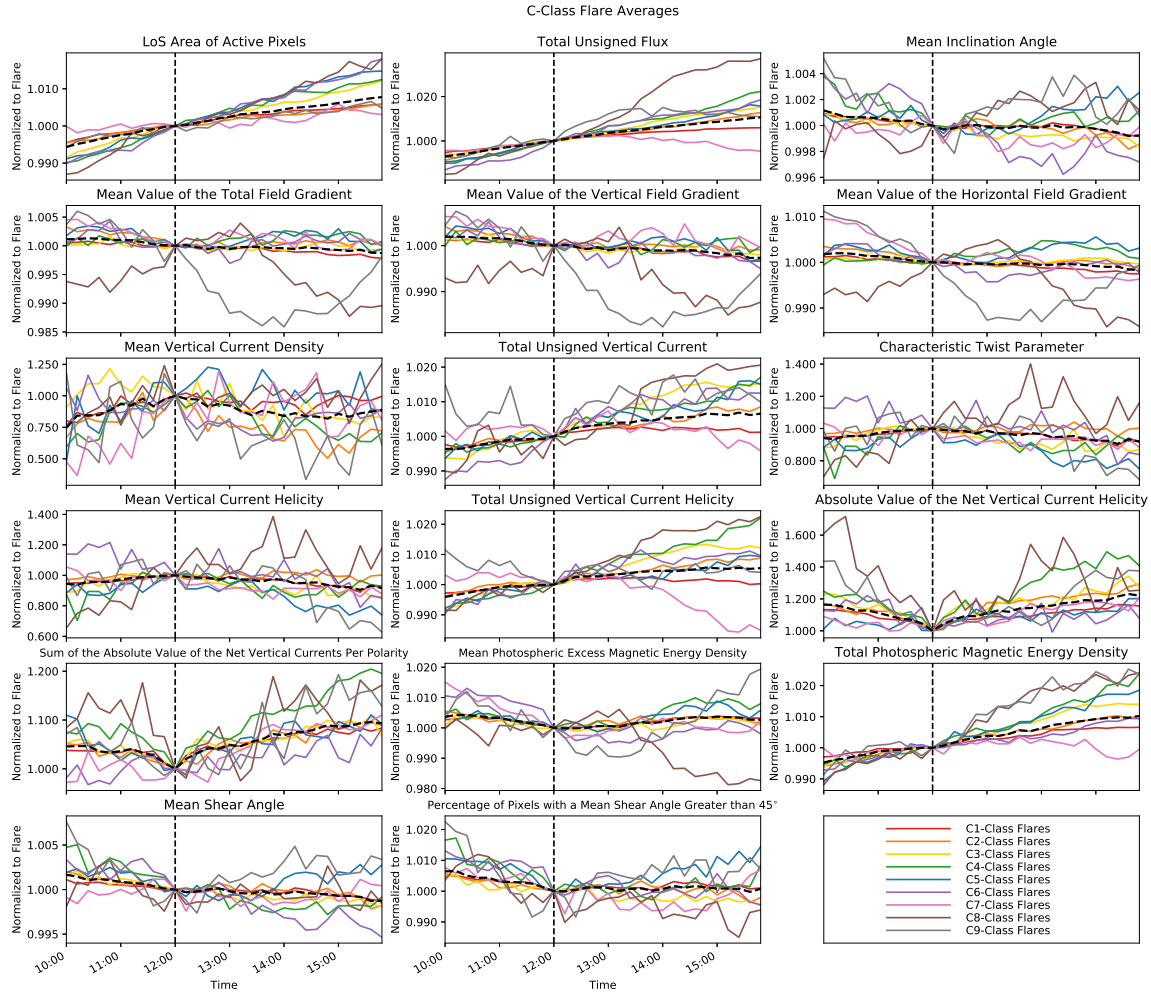
Figure 29. Epoch analysis for C-Class flares between May 2010 and September 2019. All data are normalized to the values at the time of the flare, which is identified as the dashed vertical line. Strengths of flares are separated by corresponding colors. The data are averaged for all events in the associated flare class. Flares outside of three standard deviations from the average and outside of $70°$ heliographic longitude are excluded as outliers. SHARP data are acquired from JSOC using the Python notebook created by Glogowski and Bobra (2016) and flare times are identified by SWPC (2019).
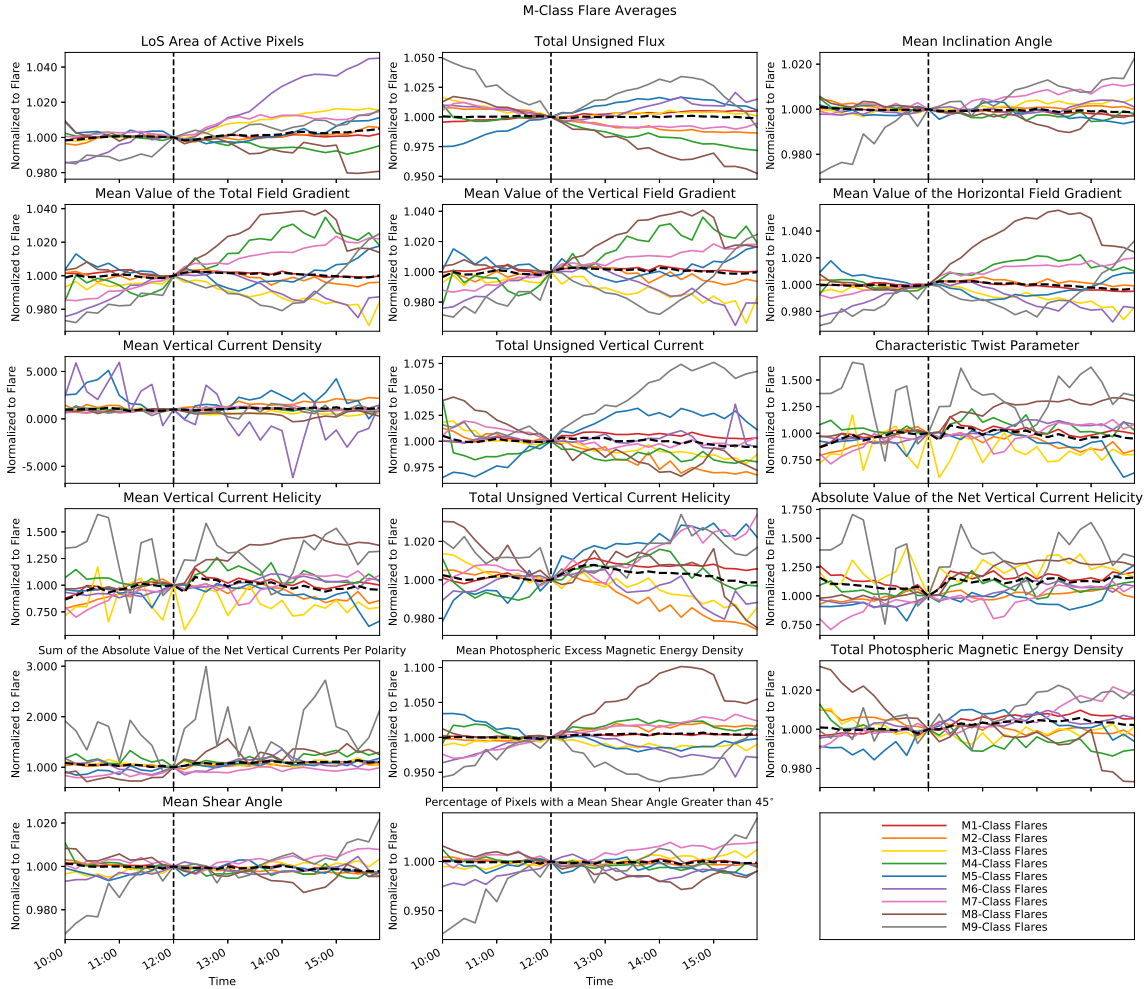
Figure 30. Epoch analysis for M-Class flares between May 2010 and September 2019. All data are normalized to the values at the time of the flare, which is identified as the dashed vertical line. Strengths of flares are separated by corresponding colors. The data are averaged for all events in the associated flare class. Flares outside of three standard deviations from the average and outside of $70°$ heliographic longitude are excluded as outliers. SHARP data are acquired from JSOC using the Python notebook created by Glogowski and Bobra (2016) and flare times are identified by SWPC (2019).
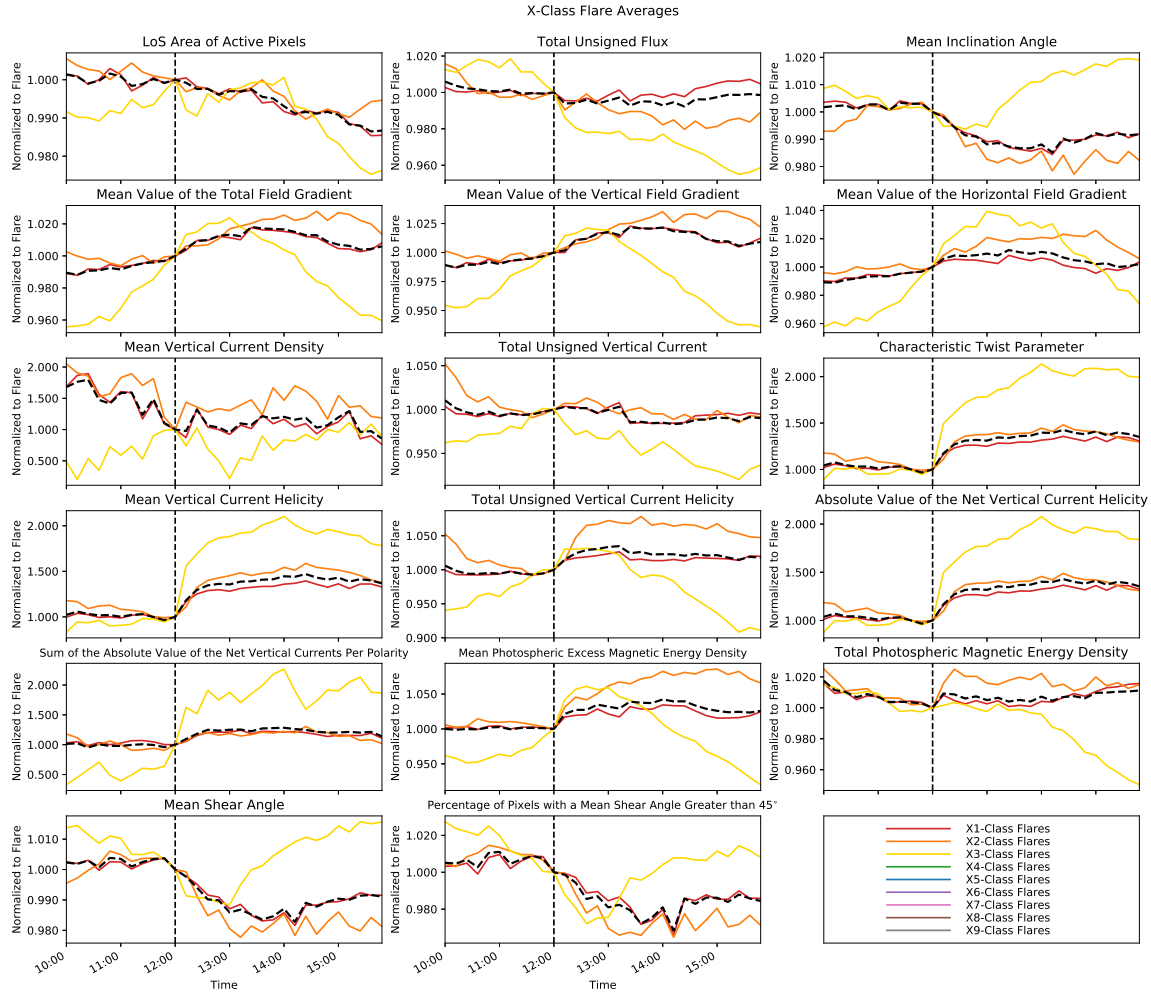
Figure 31. Epoch analysis for X-Class flares between May 2010 and September 2019. All data are normalized to the values at the time of the flare, which is identified as the dashed vertical line. Strengths of flares are separated by corresponding colors. The data are averaged for all events in the associated flare class. Flares outside of three standard deviations from the average and outside of $70°$ heliographic longitude are excluded as outliers. SHARP data are acquired from JSOC using the Python notebook created by Glogowski and Bobra (2016) and flare times are identified by SWPC (2019).

Bibliography

Bobra, M. G. and Couvidat, S. (2015). Solar Flare Prediction Using SDO/HMI Vector Magnetic Field Data with a Machine-Learning Algorithm. *The Astrophysical Journal*, 798(2):135.

Bobra, M. G., Sun, X., Hoeksema, J. T., Turmon, M., Liu, Y., Hayashi, K., Barnes, G., and Leka, K. (2014). The Helioseismic and Magnetic Imager (HMI) Vector Magnetic Field Pipeline: SHARPs–Space-Weather HMI Active Region Patches. *Solar Physics*, 289(9):3549–3578.

Carroll, B. W. and Ostlie, D. A. (2017). *An Introduction to Modern Astrophysics*. Cambridge University Press.

Chae, J., Choi, B.-K., and Park, M.-J. (2002). Chromospheric Magnetic Reconnection on the Sun. *Journal of Korean Astronomical Society*, 35:59–65.

Chae, J., Litvinenko, Y. E., and Sakurai, T. (2008). Determination of Magnetic Diffusivity from High-Resolution Solar Magnetograms. *The Astrophysical Journal*, 683(2):1153.

Criscuoli, S., Norton, A., and Whitney, T. (2017). Photometric Properties of Network and Faculae Derived from HMI Data Compensated for Scattered Light. *The Astrophysical Journal*, 847(2):93.

Eastwood, J., Biffis, E., Hapgood, M., Green, L., Bisi, M., Bentley, R., Wicks, R., McKinnell, L.-A., Gibbs, M., and Burnett, C. (2017). The Economic Impact of Space Weather: Where Do We Stand? *Risk Analysis*, 37(2):206–218.

Gibson, S., Leka, K., and Kazachenko, M. (2019). Personal conversation on 30 October 2019.

Glogowski, K. and Bobra, M. G. (2016). A New Python Module for Accessing HMI and AIA Data. `http://hmi.stanford.edu/hminuggets/?p=1757`, last accessed on 9 October 2019.

Goddard Space Flight Center (2020). The Impact of Flares. `https://hesperia.gsfc.nasa.gov/rhessi3/mission/science/the-impact-of-flares/index.html`, last accessed on 27 January 2020.

Gurnett, D. A. and Bhattacharjee, A. (2017). *Introduction to Plasma Physics: with Space, Laboratory and Astrophysical Applications.* Cambridge University Press.

Hoeksema, J. T., Liu, Y., Hayashi, K., Sun, X., Schou, J., Couvidat, S., Norton, A., Bobra, M., Centeno, R., Leka, K., et al. (2014). The Helioseismic and Magnetic Imager (HMI) Vector Magnetic Field Pipeline: Overview and Performance. *Solar Physics*, 289(9):3483–3530.

International Bureau of Weights and Measures (2019a). BIPM Work Programme 2016-2019: Time. `https://www.bipm.org/utils/en/pdf/BIPM-Work-Programme_2016-2019_TAI.pdf`, last accessed on 19 December 2019.

International Bureau of Weights and Measures (2019b). Circular T: 383. `https://www.bipm.org/en/bipm-services/timescales/time-ftp/Circular-T.html#nohref`, last accessed on 19 December 2019.

Joint Science Operations Center (2019a). HARP - HMI Active Region Patches. `http://jsoc.stanford.edu/jsocwiki/HARPDataSeries`, last accessed on 18 December 2019.

Joint Science Operations Center (2019b). Science Data Processing. `http://jsoc.stanford.edu/`, last accessed on 23 July 2019.

Joint Science Operations Center (2019c). SpaceWeather HMI Active Region Patch (SHARP). `http://jsoc.stanford.edu/doc/data/hmi/sharp/sharp.htm`, last accessed on 8 August 2019.

Joint Science Operations Center (2020). Line-of-Sight Magnetograms. `http://jsoc.stanford.edu/HMI/Magnetograms.html`, last accessed on 10 February 2020.

Kazachenko, M. D., Lynch, B. J., Welsch, B. T., and Sun, X. (2017). A Database of Flare Ribbon Properties from the Solar Dynamics Observatory. I. Reconnection Flux. *The Astrophysical Journal*, 845(1):49.

Kopp, R. and Pneuman, G. (1976). Magnetic Reconnection in the Corona and the Loop Prominence Phenomenon. *Solar Physics*, 50(1):85–98.

Leka, K. and Barnes, G. (2003). Photospheric Magnetic Field Properties of Flaring versus Flare-Quiet Active Regions. II. Discriminant Analysis. *The Astrophysical Journal*, 595(2):1296.

Leka, K., Barnes, G., and Wagner, E. (2018). The NWRA Classification Infrastructure: Description and Extension to the Discriminant Analysis Flare Forecasting System (DAFFS). *J. Space Weather Space Clim.*, 8:A25.

Liu, J., Lin, C.-H., Tsai, H., and Liou, Y. (2004). Ionospheric Solar Flare Effects Monitored by the Ground-Based GPS Receivers: Theory and Observation. *Journal of Geophysical Research: Space Physics*, 109(A1).

Loper, R. (2018). "Reconnection Signatures in Solar Magnetograms". *Proceedings of the 2018 AGU Fall Meeting*. SH14B-04. Washington, D.C.: AGU, 2018.

Mason, J. and Hoeksema, J. (2010). Testing Automated Solar Flare Forecasting with 13 Years of Michelson Doppler Imager Magnetograms. *The Astrophysical Journal*, 723(1):634.

National Oceanic and Atmospheric Administration (2019). Space Weather Prediction Center. `http://swpc.noaa.gov`, last accessed on last accessed on 16 September 2019.

Pevtsov, A. A., Canfield, R. C., and Zirin, H. (1996). Reconnection and Helicity in a Solar Flare. *The Astrophysical Journal*, 473(1):533.

Priest, E. (2014). *Magnetohydrodynamics of the Sun.* Cambridge University Press.

Priest, E. and Forbes, T. (2002). The Magnetic Nature of Solar Flares. *The Astronomy and Astrophysics Review*, 10(4):313–377.

Qian, L., Burns, A. G., Solomon, S. C., and Chamberlin, P. C. (2012). Solar Flare Impacts on Ionospheric Electrodyamics. *Geophysical research letters*, 39(6).

Scherrer, P. H., Schou, J., Bush, R., Kosovichev, A., Bogart, R., Hoeksema, J., Liu, Y., Duvall, T., Zhao, J., Schrijver, C., et al. (2012). The Helioseismic and Magnetic Imager (HMI) Investigation for the Solar Dynamics Observatory (SDO). *Solar Physics*, 275(1-2):207–227.

Schou, J., Scherrer, P. H., Bush, R. I., Wachter, R., Couvidat, S., Rabello-Soares, M. C., Bogart, R. S., Hoeksema, J. T., Liu, Y., Duvall, T. L., Akin, D. J., Allard, B. A., Miles, J. W., Rairden, R., Shine, R. A., Tarbell, T. D., Title, A. M., Wolfson, C. J., Elmore, D. F., Norton, A. A., and Tomczyk, S. (2012). Design and Ground Calibration of the Helioseismic and Magnetic Imager (HMI) Instrument on the Solar Dynamics Observatory (SDO). *Solar Physics*, 275(1):229–259.

Space Weather Prediction Center (2009). Implement XRS Event Detection. `http://intranet/wiki/index.php?title=GOES-NOP:PPNCR0078&oldid=11361`, last accessed on 19 December 2019.

Space Weather Prediction Center (2019). Data Archive. `ftp://ftp.swpc.noaa.gov/pub/warehouse/`, retreived on 25 September 2019.

Stanford University (2019). Helioseismic and Magnetic Imager. `http://hmi.stanford.edu/Description/hmi-overview/hmi-overview.html`, last accessed on 19 November 2019.

Verma, M. (2018). The Origin of Two X-Class Flares in Active Region NOAA 12673-Shear Flows and Head-on Collision of New and Preexisting Flux. *Astronomy & Astrophysics*, 612:A101.

Wheatland, M. (2008). The Energetics of a Flaring Solar Active Region and Observed Flare Statistics. *The Astrophysical Journal*, 679(2):1621.

REPORT DOCUMENTATION PAGE

Form Approved
OMB No. 0704–0188

1. REPORT DATE *(DD–MM–YYYY)*
26–03–2020

2. REPORT TYPE
Master's Thesis

3. DATES COVERED *(From — To)*
May 2018 — Mar 2020

4. TITLE AND SUBTITLE

DETECTION OF RECONNECTION SIGNATURES
IN SOLAR FLARES

5a. CONTRACT NUMBER

5b. GRANT NUMBER

5c. PROGRAM ELEMENT NUMBER

6. AUTHOR(S)

Whitney, Taylor Rose, 1st Lt, USAF

5d. PROJECT NUMBER

5e. TASK NUMBER

5f. WORK UNIT NUMBER

7. PERFORMING ORGANIZATION NAME(S) AND ADDRESS(ES)

Air Force Institute of Technology
Graduate School of Engineering and Management (AFIT/EN)
2950 Hobson Way
WPAFB OH 45433-7765

8. PERFORMING ORGANIZATION REPORT NUMBER

AFIT-ENP-MS-20-M-121

9. SPONSORING / MONITORING AGENCY NAME(S) AND ADDRESS(ES)

Air Force Office of Scientific Research
Attn: Dr. Julie Moses
875 North Randolph Street, STE 325, Room 3112
Arlington, VA 22203
COMM 703-696-9586
Email: julie.moses@us.af.mil

10. SPONSOR/MONITOR'S ACRONYM(S)

AFOSR/RTB1

11. SPONSOR/MONITOR'S REPORT NUMBER(S)

12. DISTRIBUTION / AVAILABILITY STATEMENT

DISTRIBUTION STATEMENT A:
APPROVED FOR PUBLIC RELEASE; DISTRIBUTION UNLIMITED.

13. SUPPLEMENTARY NOTES

14. ABSTRACT

Solar flare forecasting is limited by the current understanding of mechanisms that govern magnetic reconnection, the main physical phenomenon associated with these events. As a result, forecasting relies mainly on climatological correlations to historical events rather than the underlying physics principles. Solar physics models place the neutral point of the reconnection event in the solar corona. Correspondingly, studies of photospheric magnetic fields indicate changes during solar flares—particularly in relation to the field helicity—on the solar surface as a result of the associated magnetic reconnection. This study utilizes data from the Solar Dynamics Observatory (SDO) Helioseismic and Magnetic Imager (HMI) and SpaceWeather HMI Active Region Patches (SHARPs) to analyze full vector-field component data of the photospheric magnetic field during solar flares within a large HMI dataset (May 2010 through September 2019). This analysis is then used to identify and compare trends in the different categories of flare strengths and determine indications of the physical phenomena taking place.

15. SUBJECT TERMS

Solar Photosphere, Solar Active Region Magnetic Fields, Solar Flares, Space Weather, Solar Magnetic Reconnection

16. SECURITY CLASSIFICATION OF:

a. REPORT	b. ABSTRACT	c. THIS PAGE
U	U	U

17. LIMITATION OF ABSTRACT
U

18. NUMBER OF PAGES
79

19a. NAME OF RESPONSIBLE PERSON
Robert Loper, AFIT/ENP

19b. TELEPHONE NUMBER *(include area code)*
(937) 255-3636, x4333; Robert.Loper@afit.edu

Standard Form 298 (Rev. 8–98)
Prescribed by ANSI Std. Z39.18